

REPORT DOCUMENTATION PAGE

AFRL-SR-BL-TR-98-

18

Public reporting burden for this collection of information is estimated to average 1 hour per response, including the time for reviewing existing data sources, gathering and maintaining the data needed, and completing and reviewing the collection of information, including suggestions for reducing this burden to Washington, DC 20503.

existing data
or any other
operations and
at (0704-0188).

0135

1. AGENCY USE ONLY (Leave Blank)		2. REPORT DATE 11/30/97		REPORT TYPE AND DATES COVERED FINAL TECHNICAL REPORT, 01 APR 94 - 30 SEP97	
4. TITLE AND SUBTITLE Modeling of Cloud / Radiation Processes for Cirrus Cloud Formation				5. FUNDING NUMBERS F49620-94-1-0142	
6. AUTHOR(S) K.N. Liou, S.C. Ou, Y. Gu, P. Yang, D. Frankel					
7. PERFORMING ORGANIZATION NAME(S) AND ADDRESS(ES) UCLA Department of Atmospheric Sciences 405 Hilgard Avenue, 7127 Math Sciences Building Los Angeles, CA 90095-1565				8. PERFORMING ORGANIZATION REPORT NUMBER	
9. SPONSORING / MONITORING AGENCY NAME(S) AND ADDRESS(ES) Air Force Office of Scientific Research Bolling Air Force Base Washington DC 20332				10. SPONSORING / MONITORING AGENCY REPORT NUMBER	
11. SUPPLEMENTARY NOTES					
12a. DISTRIBUTION / AVAILABILITY STATEMENT Approval for public release; Distribution unlimited				12b. DISTRIBUTION CODE	
13. ABSTRACT (Maximum 200 words) This technical report includes five reprints and preprints of papers associated with the modeling of cirrus cloud and radiation processes as well as remote sensing of cloud optical and microphysical properties from an airborne spectrometer based on radiative transfer principles. The time-dependent two-dimensional cirrus model includes a second-order turbulence closure scheme, an advanced interactive radiative transfer scheme, and ice microphysics parameterization. This model is used to understand the physical processes governing the formation and evolution of cirrostratus clouds.					
14. SUBJECT TERMS Cirrus Cloud Model, Radiation Parameterization, Contrail, Remote Sensing				15. NUMBER OF PAGES 50	
				16. PRICE CODE	
17. SECURITY unclassified	18. SECURITY CLASSIFICATION OF THIS PAGE unclassified	19. SECURITY CLASSIFICATION OF THIS ABSTRACT unclassified	20. LIMITATION OF ABSTRACT UL		

DRIC QUALITY INSPECTED

MODELING OF CLOUD/RADIATION PROCESSES FOR CIRRUS
CLOUD FORMATION

Principal Investigator : K. N. Liou

Department of Atmospheric Sciences
University of California at Los Angeles
Los Angeles, California

FINAL TECHNICAL REPORT

F49620-94-1-0142

01 APR 94 to 30 SEP 97

30 November 1997

Publications Acknowledging the AFOSR Grant Support
(AFOSR F49620-94-1-0142)

01 APR 94 to 30 SEP 97

1. Gu, Y. and K. N. Liou, 1996: Interactions of radiation, microphysics, and turbulence in a two-dimensional cirrus cloud model. In *Current Problems in Atmospheric Radiation*, Smith and Stamnes (Eds.), A. Deepak Publishing, pp 238-241.
2. Gu, Y. and K. N. Liou, 1997 : Numerical experiment of the interactions of radiation, turbulence, and microphysics in cirrus clouds. *Proceedings of the 9th Atmospheric Radiation*, American Meteorological Society, Long Beach, CA, February 2-7, 1997, pp 97-101.
3. Frankel, D., K. N. Liou, S. C. Ou, D. P. Wiley, and P. Menzel, 1997: Observations of cirrus cloud extent and their impact to climate. *Proceedings of the 9th Atmospheric Radiation*, American Meteorological Society, Long Beach, CA, February 2-7, 1997, pp 414-417.
4. Liou, K. N., P. Yang, Y. Takano, K. Sassen, T. Charlock, and W. Arnott, 1997: On the radiative properties of contrail cirrus. *Geophys. Res. Lett.* (in press).
5. Ou, S. C., K. N. Liou, *et al.*, 1997: Airborne retrieval of cirrus cloud optical and microphysical properties using ARES 5.1-5.3 and 3.7- μm channel data. *J. Geophys. Res.* (submitted).

INTERACTIONS OF RADIATION, MICROPHYSICS, AND TURBULENCE IN A TWO-DIMENSIONAL CIRRUS CLOUD MODEL

Yu Gu * and K. N. Liou
Department of Meteorology/CARSS
University of Utah, Salt Lake City, Utah

ABSTRACT

A two-dimensional, time-dependent numerical model has been developed for the studies of the interactions among turbulence, radiation, and microphysics in cirrus clouds. The model incorporates parameterizations that account for phase changes of water and the effects of microphysical structure on the ice water vertical flux. Also included is an advanced interactive radiative transfer scheme which developed at University of Utah. To investigate the interactions of various physical processes, a complete version of the second-order turbulence closure model has been developed. Numerical simulation of a thin cirrostratus shows that the radiative processes begin to play an important role once a sufficient amount of ice water is produced. The induced turbulence has significant effects on the phase changes and the formation of ice water. Turbulence also enhances the radiative net cooling in the ice water region, which is an important mechanism for the maintenance of cirrus clouds.

1. INTRODUCTION

Ubiquitous cirrus clouds play an important role in the radiation field of the earth-atmosphere system, and hence the earth's climate. However, fundamental understanding of the mechanisms for their formation and dissipation is still extremely limited and has received substantial scientific attention of late (Liou 1992).

The simulation results of Starr and Cox (1985) show that the effects of radiative processes and vertical transports are both significant in the cirrus cloud formation and maintenance. Other cirrus cloud modeling studies (Jensen et al. 1994) used simplified parameterizations for radiative processes and have not considered turbulence effects in the model. At this point, interactions among radiative processes, turbulence and ice microphysics in cirrus clouds still remain poorly understood. In the present

paper, we develop a two-dimensional, time-dependent numerical model for the interaction studies.

2. MODEL DESCRIPTION

2.1. Governing Equations

The mean field equations governing the motions in the x-z plane based on the Boussinesq approximation can be written as follows:

$$\frac{\partial \zeta}{\partial t} = J(\zeta, \psi) - w_0 \frac{\partial \zeta}{\partial z} + g \frac{\partial}{\partial x} \left(\frac{\theta}{\theta_0} + \epsilon' q - \ell \right) + v \nabla^2 \zeta \\ + \frac{\partial^2 (\overline{u'w'})}{\partial z^2} - \frac{\partial^2 (\overline{u'w'})}{\partial x^2} + \frac{\partial^2 (\overline{u'^2})}{\partial x \partial z} - \frac{\partial^2 (\overline{w'^2})}{\partial x \partial z}, \quad (2.1)$$

$$\frac{\partial \theta}{\partial t} = J(\theta + \theta_0, \psi) - w_0 \frac{\partial (\theta + \theta_0)}{\partial z} + Q_R + Q_C + k_\theta \nabla^2 \theta \\ - \frac{\partial}{\partial z} (\overline{w'\theta'}) - \frac{\partial}{\partial x} (\overline{u'\theta'}), \quad (2.2)$$

$$\frac{\partial q}{\partial t} = J(q + q_0, \psi) - w_0 \frac{\partial (q + q_0)}{\partial z} - C + k_q \nabla^2 q \\ - \frac{\partial}{\partial z} (\overline{w'q'}) - \frac{\partial}{\partial x} (\overline{u'q'}), \quad (2.3)$$

$$\frac{\partial \ell}{\partial t} = \frac{\partial}{\partial t} \left(\ell \frac{\partial \psi}{\partial z} \right) - \frac{\partial}{\partial z} \left\{ \ell \left(\frac{\partial \psi}{\partial x} + w_0 - v \right) \right\} + C + k_\ell \nabla^2 \ell \\ - \frac{\partial}{\partial z} (\overline{w'\ell'}) - \frac{\partial}{\partial x} (\overline{u'\ell'}), \quad (2.4)$$

where the subscripts refer to the initial state, which is horizontally uniform, cloud free and at rest except for a constant vertical motion w_0 ; the unsubscripted variables are regarded as mean fields based on the initial state; variables with prime represent turbulent fluctuations; Q_R and Q_C are the potential temperature tendencies due to radiative processes and phase changes of water, respectively; v is the ice water relative fall speed; C is the sublimation between water vapor and ice water; q is water vapor specific humidity; ℓ is ice water mixing ratio; v is eddy viscosity; k_θ , k_q , k_ℓ are thermal, water vapor and ice water eddy diffusivities, respectively; ϵ' is related to the ratio of molecular weight of water to that of dry air, and other notations are conventional.

The governing equations (2.1)-(2.4) require nine turbulent fluxes, which can be predicted using the second-

* Corresponding author: Yu Gu, 819 WBB, Department of Meteorology, University of Utah, Salt Lake City, UT 84112; e-mail <yugu@climate.met.utah.edu>.

order turbulence closure model. The closure assumptions are described in Mellor and Yamada (1974) and are not given here.

2.2. Radiative Transfer Parameterizations

The radiative transfer scheme we have used is based on the delta-four-stream approximation developed by Liou et al. (1988). It can be applied to a nonhomogeneous cloudy atmosphere by dividing it into a number of layers each of which can be considered homogeneous with respect to the single-scattering albedo and phase function. A parameterization of non-gray gaseous absorption based on the correlated k-distribution method has been developed by Fu and Liou (1992). In this method, the cumulative probability g of the absorption coefficient in a spectral interval is used to replace wavenumber as an independent variable. Absorption due to H_2O , O_3 , CO_2 , and O_2 is accounted for in the solar spectrum. In the thermal infrared, absorption due to H_2O , O_3 , CO_2 , CH_4 , and N_2O is included. Using the correlated k-distribution method, 121 spectral calculations are required for each vertical profile.

A new parameterization has been developed for the calculations of the single-scattering properties for hexagonal ice crystals. In this parameterization, we have devised a mean effective size (D_e) to represent the ice crystal size distribution in radiative transfer calculations. Based on physical principles, the extinction coefficient normalized by IWC, the single-scattering albedo, and the expansion coefficients in the phase function may be expressed by a simple polynomial form in terms of $1/D_e$. The coefficients in the polynomials are determined by numerical fitting to the exact results obtained from the light scattering and absorption programs using 11 observed ice crystal size distributions (Takano and Liou 1989; Fu and Liou 1993). The single-scattering parameterization is performed for six solar and 12 IR bands. The calculations have been carried out using the unified theory of light scattering by ice crystals developed at the University of Utah for all applicable size parameters based on a combination of bullet rosettes, hollow columns, and plates.

2.3. Ice Microphysics Parameterizations

Ice water relative fall speed v is parameterized in terms of pressure as follows:

$$v(p) = v(p^*) \cdot (p^*/p)^{1/2}, \quad (2.5)$$

where $p^*=400$ mb. The reference value $v(p^*)$ is taken from the parametric relationship developed by Starr and Cox (1985).

Sublimation of vapor to ice occurs when $q_0 + q > c_0 q_s$, where $c_0=1.2$ when $\ell=0$ and $c_0=1.05$ when $\ell>0$. The amount of water vapor sublimated to ice (Δq) is

solved by iteration from the following simultaneous equations:

$$q_0 + q - \Delta q = c_0 q_s (T_0 + T^n), \quad (2.6)$$

$$L \Delta q = c_p (T^n - T), \quad (2.7)$$

where T^n is the new temperature after phase change; c_0 is taken the same value as given before. Then the sublimation between water vapor and ice water (C) and the potential temperature tendency due to phase changes of water (Q_C) can be obtained from

$$C = \Delta q / \Delta t, \quad (2.8)$$

$$Q_C = \frac{LC}{C_p \Pi_0}, \quad (2.9)$$

where $\Pi_0 = (p_0/p_r)^{R/C_p}$; $p_r=1000$ mb; and Δt is the time interval.

Sublimation of ice to vapor is diagnosed when $\ell>0$ and $q_0 + q_s < c_i q_s$, where $c_i=1.05$. The amount of ice sublimated to water vapor is diagnosed as $\Delta \ell = c \ell$, where c is a coefficient related to the saturation ratio and $0 \leq c \leq 1$. The terms C and Q_C can be calculated from Eqs. (2.8) and (2.9), but Δq must be set to be $-\Delta \ell$. The phase change diagnoses are performed at five minutes intervals during a simulation.

2.4. Boundary Conditions

Cyclic boundary conditions are specified at the lateral boundaries. The upper and lower boundaries are set so that the evolving disturbances remain isolated within the domain, i.e.,

$$\zeta = 0, \psi = 0, \ell = 0,$$

and

$$\frac{\partial \theta}{\partial t} = -w_0 \frac{\partial \theta_0}{\partial z}, \quad \frac{\partial q}{\partial t} = w_0 \frac{\partial q_0}{\partial z}.$$

For the eddy diffusion terms, the cross-boundary transport is simply specified as zero as follows:

$$\frac{\partial \xi}{\partial z} = \frac{\partial \theta}{\partial z} = \frac{\partial q}{\partial z} = \frac{\partial \ell}{\partial z} = 0$$

The second-order moments are set to zero at the vertical boundaries.

Comprehensive numerical schemes have been designed for the simulation of cloud formation but for brevity, they are not given here.

3. CIRrus CLOUD SIMULATION

Figure 1a shows the vertical profile of the horizontally averaged IWC at four time steps. At $t=10$ min, IWC increases rapidly to its maximum value due to the initial dynamic and thermodynamic forcings. As ice water falls into the drier lower region, sublimation occurs and the simulated IWC decreases. Toward the end of the simulation, IWC reaches to a steady state. Also shown is

the maximum value of the simulated horizontally averaged IWC which is about 0.044 g/m^3 at $t=10 \text{ min}$, much larger than the value 0.027 g/m^3 reported by Starr and Cox (1985). The potential temperature tendency due to phase changes (Q_c) maintains positive in the ice water region, implying a net ice water formation in this region. In the lower region, however, a net ice destruction is found ($Q_c < 0$). At first, formation is much stronger than destruction, but at $t=20 \text{ min}$, destruction surpasses generation. Finally, the generation of ice water is balanced by the destruction and the transport to the lower level. The maximum radiative cooling is located at the cloud top, while the subcloud region shows radiative warming. Radiative cooling and warming decrease with time and reach to a quasi-steady state at the end of the simulation (Fig. 1c).

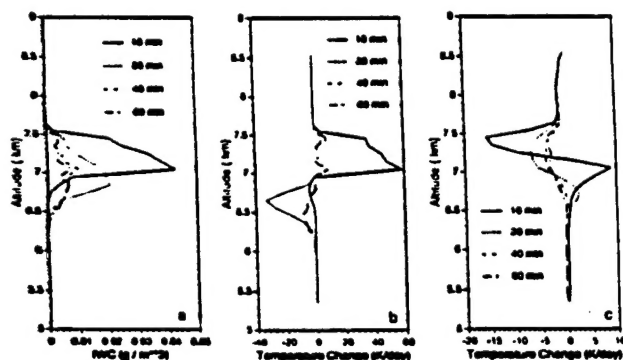


Fig.1. Vertical profiles of horizontally averaged IWC (a), potential temperature tendency due to phase changes (b), and radiation (c) at four time steps.

During the cirrus cloud formation period, the latent heat release in the ice water region is much larger than the net radiative cooling in response to the initial conditions. After about $t=20 \text{ min}$ of the simulation, these two values become comparable, indicating that the radiative processes begin to play a significant role when a sufficient amount of ice water is produced (Fig. 1b and Fig. 1c).

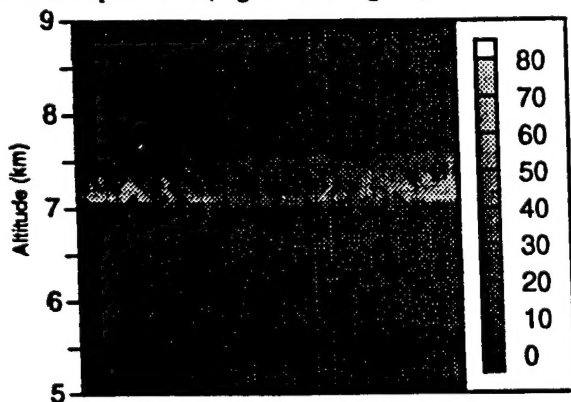


Fig.2. Image of IWC (in mg/m^3) at $t=10 \text{ min}$.

Contour map of IWC at $t=10 \text{ min}$ is shown in Fig. 2. Updraft as large as 40 cm/s is simulated and the maximum simulated IWC located at about 7 km is about 0.055 g/m^3 , both match the observed values (Heymsfield 1975).

4. INTERACTIONS OF RADIATION, TURBULENCE, AND ICE MICROPHYSICS

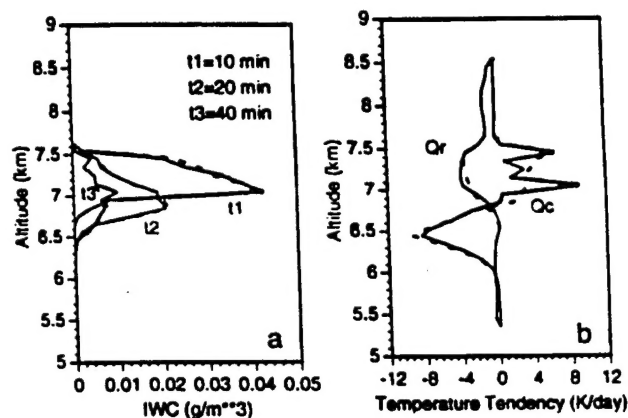


Fig.3. Vertical profiles of the horizontally averaged IWC at three time steps (a); potential temperature tendency due to phase changes (Q_c) and radiation (Q_r) at $t=40 \text{ min}$ during simulations with a(solid) and without (dashed) turbulence.

Vertical profiles of the horizontally averaged IWC at three time steps as well as the latent heat and net radiative heating/cooling at $t=40 \text{ min}$ with and without turbulence are present in Fig. 3. The primary role of turbulence is to modulate the supersaturation condition as to affect ice nucleation and consequently the rate at which water vapor is converted to ice. When the cirrus cloud begins to form, sublimation of water vapor to ice water is primarily determined by the initial forcings. Turbulent and radiative processes appear to be not important and so the differences between the two experiments are small. After $t=20 \text{ min}$, the direct effects of turbulence on phase changes become apparent. Q_c increases by about 3°C/day due to the presence of turbulence and the corresponding horizontally averaged IWC increases by 2 mg/m^3 (Fig. 3a). At this stage, however, the influence of turbulence on radiative processes is still absent (figures are not shown here). During the maintenance period of the cirrus life cycle, feedback of turbulence to radiative heating/cooling becomes significant (Fig. 3b). Due to the including of turbulence in the model, the maximum net radiative cooling in the ice water region is enhanced by about 1°C/day , which is 25% of the total cooling rate. At the same time, Q_c increases by

about $6^{\circ}\text{C}/\text{day}$. As a result, IWC increases by about $5\text{ mg}/\text{m}^3$ (Fig. 3a). Fig. 3b reveals that the rate of net ice formation at this level is greater with the turbulence, which is consistent with the IWC difference. Also, turbulence modifies the static stability through radiative processes. It is seen that the radiative stabilization in the upper portion of the cloud generation region is more apparent in the case without turbulence.

We have also carried out two other experiments with the inclusion of turbulence but with and without incorporating radiation in the model. The results are shown in Fig. 4. Radiation effects appear to be not substantial at first. However, at about $t=20\text{ min}$ in the ice water region, radiation enhances the latent heat by about $8^{\circ}\text{C}/\text{day}$, implying that the condensation and hence the increase of the rate of net formation are both strengthened through both direct effects from ice microphysics and indirect effects from the induced entrainment and mixing (Fig. 4b). The corresponding IWC differences, however, are much smaller than that produced from the turbulent effect (Fig. 4a). Comparing Fig. 3a and Fig. 4a, we see that the induced turbulence, which feeds back to the radiative processes, is more significant in the formation of ice water, as evidenced from the larger IWC differences.

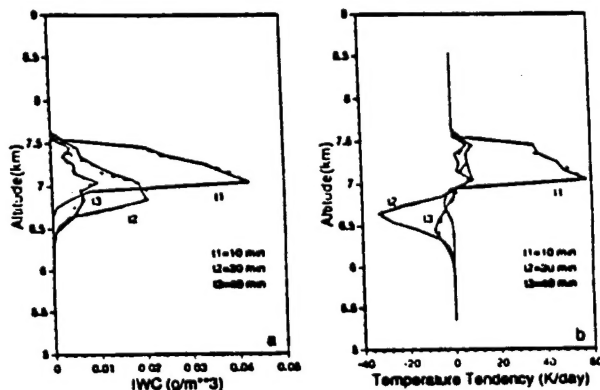


Fig. 4. Vertical profiles of the horizontally averaged IWC (a) and latent heat (b) for experiments with (solid) and without (dashed) radiation.

In summary, the simulation results in terms of a number of physical parameters denoted above are sensitive to turbulent and the radiative processes. Turbulence directly affects ice microphysics by producing higher supersaturation. Also, it can influence radiation by enhancing the net cooling rate and reducing the radiative stabilization.

5. CONCLUSIONS

A two-dimensional numerical model has been developed to investigate the interactions among radiative

processes, turbulence, and ice microphysics and their effects on the formation of cirrus clouds. Numerical results show that cirrus clouds are first formed by the dynamic and thermodynamic forcings. Once a sufficient amount of ice water is produced in the atmosphere, radiative processes begin to play an important role through its net cooling effect on the cloud top. The induced turbulence has significant effects on the phase changes and the ice water formation. Also, turbulence affects the radiative processes by increasing the net radiative cooling in the ice water generation region, which is important in the maintenance of cirrus clouds.

ACKNOWLEDGMENTS

Research work reported in this paper has been supported by the Air Force Office of Scientific Research under Grant F49820-94-1-0142.

REFERENCES

- Fu, Q., and K. N. Liou, 1992: On the correlated k-distribution method for radiative transfer in nonhomogeneous atmosphere. *J. Atmos. Sci.*, **49**, 2139-2156.
- Fu, Q., and K. N. Liou, 1993: Parameterization of the radiative properties of cirrus clouds. *J. Atmos. Sci.*, **50**, 2008-2025.
- Heymsfield, A. J., 1975: Cirrus uncinus generating cells and the evolution of cirriform clouds. Part I: Air craft observations of the growth of the ice phase. *J. Atmos. Sci.*, **32**, 799-808.
- Jensen, E. J., O. B. Toon, D. L. Westphal, S. Kinne, and A. J. Heymsfield, 1994: Microphysical modeling of cirrus: 1. Comparison with 1986 FIRE IFO Measurements. 2. Sensitivity studies. *J. Geophys. Res.*, **99**, 10421-10454.
- Liou, K. N., Q. Fu, and T. P. Ackerman, 1988: A simple formulation of the δ -four-stream approximation for radiative transfer parameterizations. *J. Atmos. Sci.*, **45**, 1940-1947.
- Liou, K. N., 1992: *Radiation and Cloud Processes in the Atmosphere: Theory, Observation, and Modeling*. Oxford University Press, New York, 487pp.
- Mellor, G. L., and T. Yamada, 1974: A hierarchy of turbulence closure models for planetary boundary layer. *J. Atmos. Sci.*, **31**, 1791-1806.
- Starr, D. O'C., and S. K. Cox, 1985: Cirrus clouds. Part I: Cirrus cloud model. *J. Atmos. Sci.*, **42**, 2663-2681.
- Takano, Y., and K. N. Liou, 1989: Solar radiative transfer in cirrus clouds. Part I: Single-scattering and optical properties of hexagonal ice crystals. *J. Atmos. Sci.*, **46**, 3-19.

NUMERICAL EXPERIMENTS ON THE INTERACTIONS OF RADIATION, TURBULENCE, AND MICROPHYSICS IN CIRRUS CLOUDS

Yu Gu * and K. N. Liou
Department of Meteorology/CARSS
University of Utah, Salt Lake City, Utah

ABSTRACT

A two-dimensional, time-dependent numerical model has been developed for the studies of the interactions among turbulence, radiation, and microphysics in cirrus clouds. The model focuses on cloud-scale processes with a 100 m grid resolution and incorporates parameterizations that account for phase changes of water and the effects of microphysical structure on the ice water vertical flux. Also included is an advanced interactive radiative transfer scheme, which employs the δ -four-stream approximation for radiative transfer, the correlated k -distribution method for nongray gaseous absorption, and the scattering and absorption properties of hexagonal ice crystals. To investigate the interactions of turbulence, radiative transfer, and ice microphysics and their contributions to the evolution of cirrus clouds, a complete version of the second-order turbulence closure model that includes prognostic equations for all the second moments has been developed. Numerical simulation of a thin cirrostratus shows that the radiative processes begin to play an important role once a sufficient amount of ice water is produced. The induced turbulence has significant effects on the phase changes and the formation of ice water. Turbulence also enhances the radiative net cooling in the ice water region, which is an important mechanism for the maintenance of cirrus clouds.

1. INTRODUCTION

Ubiquitous cirrus clouds play an important role in the radiation field of the earth-atmosphere system, and hence the earth's climate. However, fundamental understanding of the mechanisms for their formation and dissipation is still extremely limited and has received substantial scientific attention of late (Liou 1992).

Several attempts have been made to develop numerical models to investigate the role of various physical processes in the life cycle of a cirrus cloud. The results of Starr and Cox (1985) show that the effects of radiative processes and vertical transports are both significant in the cirrus cloud formation and maintenance. Other cirrus cloud modeling studies (Heymsfield et al. 1989; Jensen et al. 1994) used simplified parameterizations for radiative processes and have not considered turbulence effects in the model. At this point, interactions among radiative processes, turbulence and ice microphysics and how they contribute to the formation, maintenance and dissipation of

cirrus clouds still remain poorly understood. Although it is known that radiative cooling (and indirectly mixing and cloud-top entrainment) is dependent on cloud microphysics, the effect of the induced turbulence on ice microphysics, which can feed back to the radiative cooling, has not been previously examined. This feedback process could have an important role in the maintenance of cirrus clouds (Curry 1985).

In this paper, we develop a two-dimensional, time-dependent numerical model to investigate the interactions among radiative processes, turbulence, and ice microphysics, and their effects on the formation and maintenance of a cirrus cloud. An advanced interactive radiative transfer scheme for cirrus clouds (Fu and Liou 1993) has been included in the model. In addition, a complete version of the second-order turbulence closure model (Level-4 model) which contains the prognostic equations for all of the second moments has been developed and incorporated into the present model for interaction and feedback studies. In Section 2, we describe the numerical model that includes turbulent transfer and radiative processes. Simulation results are presented in Section 3. In Section 4, we discuss the interactions of various physical processes and their effects on the life cycle of a cirrus cloud. Summary and conclusions are given in Section 5.

2. MODEL DESCRIPTION

2.1. Governing Equations

The mean field equations governing the motions in the x - z plane based on the Boussinesq approximation can be written as follows:

$$\frac{\partial \zeta}{\partial t} = J(\zeta, \psi) - w_0 \frac{\partial \zeta}{\partial z} + g \frac{\partial}{\partial x} \left(\frac{\theta}{\theta_0} + \epsilon' q - \ell \right) + v \nabla^2 \zeta + \frac{\partial^2 (\overline{u'w'})}{\partial z^2} - \frac{\partial^2 (\overline{u'w'})}{\partial x^2} + \frac{\partial^2 (\overline{u'^2})}{\partial x \partial z} - \frac{\partial^2 (\overline{w'^2})}{\partial x \partial z}, \quad (2.1)$$

$$\frac{\partial \theta}{\partial t} = J(\theta + \theta_0, \psi) - w_0 \frac{\partial (\theta + \theta_0)}{\partial z} + Q_R + Q_C + k_\theta \nabla^2 \theta - \frac{\partial}{\partial z} (\overline{w'\theta'}) - \frac{\partial}{\partial x} (\overline{u'\theta'}), \quad (2.2)$$

$$\frac{\partial q}{\partial t} = J(q + q_0, \psi) - w_0 \frac{\partial (q + q_0)}{\partial z} - C + k_q \nabla^2 q - \frac{\partial}{\partial z} (\overline{w'q'}) - \frac{\partial}{\partial x} (\overline{u'q'}), \quad (2.3)$$

$$\frac{\partial \ell}{\partial t} = \frac{\partial}{\partial x} \left(\ell \frac{\partial \psi}{\partial z} \right) - \frac{\partial}{\partial z} \left\{ \ell \left(\frac{\partial \psi}{\partial x} + w_0 - v \right) \right\} + C + k_\ell \nabla^2 \ell - \frac{\partial}{\partial z} (\overline{w'\ell'}) - \frac{\partial}{\partial x} (\overline{u'\ell'}), \quad (2.4)$$

* Corresponding author address: Yu Gu, 819 WBB, Department of Meteorology, University of Utah, Salt Lake City, UT 84112; e-mail <yugu@climate.met.utah.edu>.

where the subscripts refer to the initial state, which is horizontally uniform, cloud free and at rest except for a constant vertical motion w_0 ; the unsubscripted variables are regarded as mean fields based on the initial state; variables with prime represent turbulent fluctuations; Q_R and Q_C are the potential temperature tendencies due to radiative processes and phase changes of water, respectively; v is the ice water relative fall speed; C is the sublimation between water vapor and ice water; q is water vapor specific humidity; ℓ is ice water mixing ratio; ν is eddy viscosity; k_θ , k_q , k_ℓ are thermal, water vapor and ice water eddy diffusivities, respectively; ϵ' is related to the ratio of molecular weight of water to that of dry air, and other notations are conventional.

2.2. Turbulent Flux Equations

The governing equations (2.1)-(2.4) require nine turbulent fluxes, which can be predicted using the second-order closure based on 12 prognostic equations for the second moments. The closure assumptions are described in Mellor and Yamada (1974). The mean Reynolds stress model equations are given by

$$\begin{aligned} \frac{\partial \overline{u_i' u_j'}}{\partial t} - \frac{\partial}{\partial x_k} \left[q' \lambda_1 \left(\frac{\partial \overline{u_i' u_j'}}{\partial x_k} + \frac{\partial \overline{u_i' u_k'}}{\partial x_j} + \frac{\partial \overline{u_j' u_k'}}{\partial x_i} \right) \right] \\ = -\overline{u_k' u_i'} \frac{\partial u_j}{\partial x_k} - \overline{u_k' u_j'} \frac{\partial u_i}{\partial x_k} - \frac{2}{3} \frac{q'^3}{\Lambda_1} \delta_{ij} \\ - \frac{q'}{3 \ell_1} (\overline{u_i' u_j'} - \frac{\delta_{ij}}{3} q'^2) + c_1' q'^2 \left(\frac{\partial u_i}{\partial x_j} + \frac{\partial u_j}{\partial x_i} \right) \\ - \beta (g_j \overline{u_i' \theta'} + g_i \overline{u_j' \theta'}), \end{aligned} \quad (2.5)$$

$$\frac{\partial \overline{\theta'^2}}{\partial t} - \frac{\partial}{\partial x_k} \left(q' \lambda_2 \frac{\partial \overline{\theta'^2}}{\partial x_k} \right) = -2 \overline{u_k' \theta'} \frac{\partial \theta}{\partial x_k} - 2 \frac{q'}{\Lambda_2} \overline{\theta'^2}, \quad (2.6)$$

$$\begin{aligned} \frac{\partial \overline{u_j' \theta'}}{\partial t} - \frac{\partial}{\partial x_k} \left[q' \lambda_3 \left(\frac{\partial \overline{u_j' \theta'}}{\partial x_k} + \frac{\partial \overline{u_k' \theta'}}{\partial x_j} \right) \right] \\ = -\overline{u_j' u_k'} \frac{\partial \theta}{\partial x_k} - \overline{u_k' \theta'} \frac{\partial u_j}{\partial x_k} - \beta g_j \overline{\theta'^2} - \frac{q'}{3 \ell_2} \overline{u_j' \theta'}, \end{aligned} \quad (2.7)$$

Equation (2.5) contains three prognostic equations for $\overline{u'^2}$, $\overline{u'w'}$, and $\overline{w'^2}$, while Eq. (2.7) contains two equations for $\overline{u'\theta'}$ and $\overline{w'\theta'}$. The turbulent fluxes with respect to q and ℓ can be expressed by following Eqs. (2.6) and (2.7) and are not given here. In these equations, β is the coefficient of thermal expansion; $g_j = (0, 0, -g)$ the gravity vector; q' is the square root of the turbulence kinetic energy; c_1' is a constant taken from Mellor and Yamada (1974); and λ_1 , λ_2 , λ_3 , ℓ_1 , ℓ_2 , and Λ_1 , Λ_2 are all length parameters which are related to length scale l .

For the length scale, we have adopted the interpolation formula developed by Blackadar (1962) in the form

$$l = \frac{kz}{1 + kz/l_0}, \quad (2.8)$$

where k is von Karman constant; $l_0 = 0.00027 * U_G / f$; f is the Coriolis parameter; and U_G is the geostrophic wind velocity, which is set at a constant value 16 m/s.

2.3. Radiative Transfer Parameterizations

We have used the radiation parameterization scheme developed at the University of Utah for the cirrus cloud modeling studies. This scheme is based on the delta-four-stream approximation developed by Liou et al. (1988). It can be applied to a nonhomogeneous cloudy atmosphere by dividing it into a number of layers each of which can be considered homogeneous with respect to the single-scattering albedo and phase function. Using the boundary conditions at the top and bottom of the atmosphere and the continuity requirements at the interface of the predivided homogeneous layers, the unknown coefficients in the analytic solution for the transfer equation can be determined, leading to the calculations of fluxes.

A parameterization of non-gray gaseous absorption based on the correlated k -distribution method has been developed by Fu and Liou (1992). In this method, the cumulative probability g of the absorption coefficient in a spectral interval is used to replace wavenumber as an independent variable. Monochromatic solutions of the radiative transfer equation for the multiple-scattering atmosphere can be used in connection with a given g . The minimum number of quadrature points in the g space ranges from one to about ten for different absorbing gases in different spectral regions.

The solar and IR spectra are divided into a number of spectral intervals according to the location of the gaseous absorption bands. Absorption due to H_2O , O_3 , CO_2 , and O_2 is accounted for in the solar spectrum. In the thermal infrared, absorption due to H_2O , O_3 , CO_2 , CH_4 , and N_2O is included. Using the correlated k -distribution method, 121 spectral calculations are required for each vertical profile.

A new parameterization has been developed for the calculations of the single-scattering properties for hexagonal ice crystals. In this parameterization, we have devised a mean effective size (D_e), which is defined as the mean width weighted by the cross-section area, to represent the ice crystal size distribution in radiative transfer calculations. Based on physical principles, the extinction coefficient normalized by IWC, the single-scattering albedo, and the expansion coefficients in the phase function may be expressed by a simple polynomial form in terms of $1/D_e$. The coefficients in the polynomials are determined by numerical fitting to the exact results obtained from the light scattering and absorption programs using 11 observed ice crystal size distributions (Takano and Liou 1989; Fu and Liou 1993). The single-scattering parameterization is performed for six solar and 12 IR bands. The calculations have been carried out using the unified theory of light scattering by ice crystals developed at the University of Utah for all applicable size parameters based on a combination of bullet rosettes, hollow columns, and plates.

The radiation parameterization program is driven by the mean effective size and ice water path, which is the product of IWC and the cloud thickness. In the present cirrus cloud model, the ice crystal size is not predicted and is prescribed using a typical cirrostratus value.

2.4. Ice Microphysics Parameterizations

Ice water relative fall speed v is parameterized in terms of pressure as follows:

$$v(p) = v(p^*) \cdot (p^* / p)^K, \quad (2.9)$$

where $p^*=400$ mb. The reference value $v(p^*)$ is taken from the parametric relationship developed by Starr and Cox (1985).

Sublimation of vapor to ice occurs when $q_0 + q > c_0 q_s$, where $c_0=1.2$ when $\ell=0$ and $c_0=1.05$ when $\ell>0$. The amount of water vapor sublimated to ice (Δq) is solved by iteration from the following simultaneous equations:

$$q_0 + q - \Delta q = c_0 q_s (T_0 + T^*), \quad (2.10)$$

$$L \Delta q = c_p (T^* - T), \quad (2.11)$$

where T^* is the new temperature after phase change; c_0 is taken the same value as given before. Then the sublimation between water vapor and ice water (C) and the potential temperature tendency due to phase changes of water (Q_c) can be obtained from

$$C = \Delta q / \Delta t, \quad (2.12)$$

$$Q_c = \frac{LC}{c_p \Pi_0}, \quad (2.13)$$

where $\Pi_0 = (p_0 / p_r)^{R/C_p}$; $p_r=1000$ mb; and Δt is the time interval.

Sublimation of ice to vapor is diagnosed when $\ell>0$ and $q_0 + q < c_1 q_s$, where $c_1=1.05$. The amount of ice sublimated to water vapor is diagnosed as $\Delta \ell = c \ell$, where c is a coefficient related to the saturation ratio and $0 \leq c \leq 1$. The terms C and Q_c can be calculated from Eqs. (2.12) and (2.13), but Δq must be set to be $-\Delta \ell$. The phase change diagnoses are performed at five minutes intervals during a simulation.

2.5. Boundary Conditions And Numerical Methods

Cyclic boundary conditions are specified at the lateral boundaries. The upper and lower boundaries are set so that the evolving disturbances remain isolated within the domain, i.e.,

$$\zeta = 0, \quad \psi = 0, \quad \ell = 0,$$

and

$$\frac{\partial \theta}{\partial t} = -w_0 \frac{\partial \theta_0}{\partial z}, \quad \frac{\partial q}{\partial t} = w_0 \frac{\partial q_0}{\partial z}.$$

For the eddy diffusion terms, the cross-boundary transport is simply specified as zero as follows:

$$\frac{\partial \xi}{\partial z} = \frac{\partial \theta}{\partial z} = \frac{\partial q}{\partial z} = \frac{\partial \ell}{\partial z} = 0$$

The second-order moments are set to zero at the vertical boundaries.

The dimensions of the computational domain used are 3.2 km in the vertical and 6.4 km in the horizontal with a uniform horizontal and vertical resolution of 100 m. The nonlinear term of the vorticity equation (2.1) is evaluated by the finite-difference scheme in terms of the flux form using Arakawa's (1966) nine-point Jacobian, which conserves both the mean kinetic energy and mean square vorticity. The nonlinear terms in equations (2.2) and (2.3) are computed following the method developed by Lilly (1965). The terms in Eq. (2.4) are obtained by an upstream flux scheme. Equations (2.1)-(2.3) are solved by using the second-order Adams-Bashforth scheme, except that the Euler forward scheme is used for the initial time step. The Euler forward scheme is also used for the solution of ice water denoted in Eq. (2.4) to ensure computational stability.

3. CIRRUS CLOUD SIMULATION

The initial thermal stratifications used in the present model are a number of specified lapse rates in various vertical regions, which are expressed in terms of the pseudo-adiabatic lapse rate governing the unmixed vertical displacements at ice saturation, typical of thin cirrus cloud layers. There is no ice water initially. The disturbance is initiated through the prescribed potential temperature perturbation at all grid points in the layer from $z=6.55$ to 7.55 km, with a maximum and a mean value of 0.1 and 0.05°C , respectively.

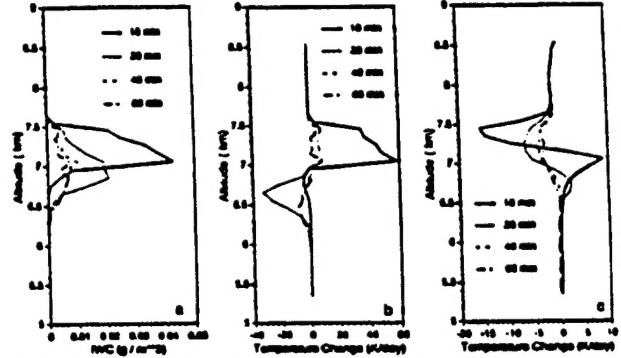


Fig. 1. Vertical profiles of horizontally averaged IWC (a), the potential temperature tendency due to phase changes (b), and radiation (c) at four time steps.

Figure 1a shows the vertical profile of the horizontally averaged IWC at four time steps during a cirrus cloud simulation. At $t=10$ min, IWC increases rapidly to its maximum value due to the initial dynamic and thermodynamic forcings. Because the values of the ice water relative fall speed at that time are larger than the updraft speeds, ice water falls to levels below and the location of the maximum IWC shifts from 7.15 km at $t=10$ min to 6.95 km at $t=20$ min. As ice water falls into the drier lower region, sublimation occurs and the simulated IWC decreases. Toward the end of the simulation, IWC reaches to a steady state in which the formation and destruction of ice water is balanced. Also shown is the maximum value of the simulated horizontally averaged IWC which is about 0.044 g/m^3 at $t=10$ min, located at about 7 km, much larger than the value 0.027 g/m^3 reported by Starr and Cox (1985). These processes are also clearly illustrated from the vertical profile of potential temperature tendency due to phase changes of water (Q_c) (Fig. 1b). Q_c maintains positive in the ice water region, implying a net ice water formation in this region. In the lower region, however, a net ice destruction is found ($Q_c < 0$). At first, formation is much stronger than destruction, but at $t=20$ min, destruction surpasses generation. Finally, the generation of ice water is balanced by the destruction and the transport to the lower level. The vertical profiles of net radiative cooling/warming at different time steps are shown in Fig. 1c. The maximum radiative cooling is located at the cloud top, while the subcloud region shows radiative warming. Radiative cooling and warming decrease with time and reach to a quasi-steady state at the end of the simulation.

Vertical profiles of the potential temperature change due to phase change, solar, infrared and net radiation are illustrate in Fig. 2. During the cirrus cloud formation

period, the latent heat release in the ice water region is much larger than the net radiative cooling in response to the initial conditions. After about $t=20$ min of the simulation, these two values become comparable, indicating that the radiative processes begin to play a significant role when a sufficient amount of ice water is produced.

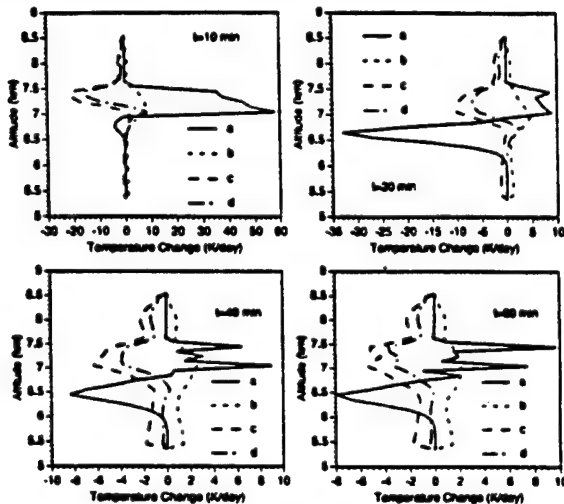


Fig.2. Vertical profiles of temperature change due to (a) phase changes, (b) solar, (c) infrared, and (d) net radiative processes at four time steps.

Contour map of IWC at $t=10$ min is shown in Fig. 3. Updraft as large as 40 cm/s is simulated and the maximum simulated IWC located at about 7 km is about 0.055 g/m^3 , both match the observed values (Heymsfield 1975).

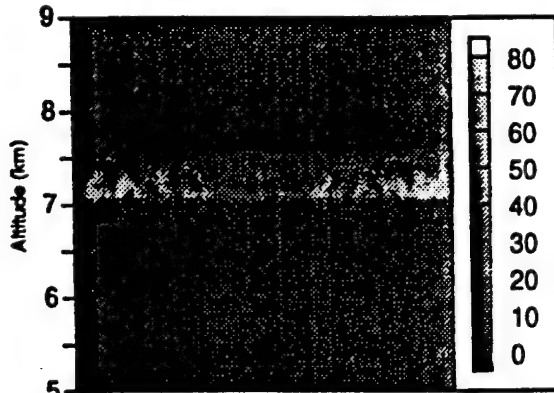


Fig.3. Image of IWC (in mg/m^3) at $t=10$ min.

From the preceding discussion, it is clear that the radiative processes play an important role in the life cycle of a cirrus cloud, especially in the maintenance period. The present model also produces more ice water than that reported in Starr and Cox (1985) in whose model the effects of turbulence and radiation have not been treated comprehensively.

4. INTERACTIONS OF RADIATION, TURBULENCE, AND ICE MICROPHYSICS

In this section, we investigate the interactions and the feedback of the entrainment and mixing to the radiative cooling during the simulation of the life cycle of a cirrus

cloud. Vertical profiles of the horizontally averaged IWC at three time steps as well as the latent heat and net radiative heating/cooling at $t=40$ min with and without turbulence are present in Fig. 4. The primary role of turbulence is to modulate the supersaturation condition as to affect ice nucleation and consequently the rate at which water vapor is converted to ice. When the cirrus cloud begins to form, sublimation of water vapor to ice water is primarily determined by the initial forcings. Turbulent and radiative processes appear to be not important and so the differences between the two experiments are small. After $t=20$ min, the direct effects of turbulence on phase changes become apparent. Q_c increases by about 3°C/day due to the presence of turbulence and the corresponding horizontally averaged IWC increases by 2 mg/m^3 (Fig. 4a). At this stage, however, the influence of turbulence on radiative processes is still absent (figures are not shown here). During the maintenance period of the cirrus life cycle at $t=40$ min, feedback of turbulence to radiative heating/cooling becomes significant (Fig. 4b). Solar heating is less than IR cooling throughout all layers, resulting in net cooling. Due to the including of turbulence in the model, the maximum net radiative cooling in the ice water region is enhanced by about 1°C/day , which is 25% of the total cooling rate. At the same time, Q_c increases by about 6°C/day . As a result, IWC increases by about 5 mg/m^3 (Fig. 4a). Fig. 4b reveals that the rate of net ice formation at this level is greater with the turbulence, which is consistent with the IWC difference. Also, turbulence modifies the static stability through radiative processes. It is seen that the radiative stabilization in the upper portion of the cloud generation region is more apparent in the case without turbulence.

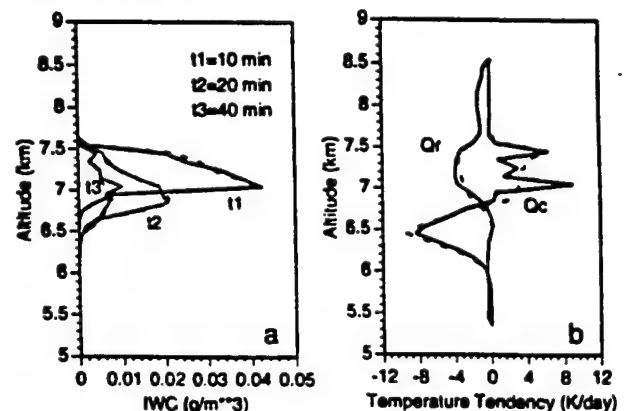


Fig.4. Vertical profiles of the horizontally averaged IWC at three time steps (a), potential temperature tendency due to phase changes (Q_c) and radiation (Q_r) at $t=40$ min during simulations with (solid) and without (dashed) turbulence.

We have also carried out two other experiments with the inclusion of turbulence but with and without incorporating radiation in the model. The results are shown in Fig. 5. Radiation effects appear to be not substantial at first. However, at about $t=20$ min in the ice water region, radiation enhances the latent heat by about 8°C/day , implying that the condensation and hence the increase of the rate of net formation are both strengthened through both direct effects from ice microphysics and indirect effects from the induced entrainment and mixing

(Fig. 5b). The corresponding IWC differences, however, are much smaller than that produced from the turbulent effect (Fig. 5a). Comparing Fig. 4a and Fig. 5a, we see that the induced turbulence, which feeds back to the radiative processes, is more significant in the formation of ice water, as evidenced from the larger IWC differences.

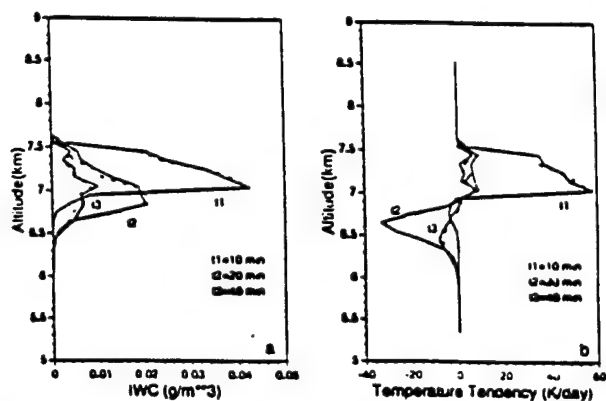


Fig. 5. Vertical profiles of the horizontally averaged IWC (a) and latent heat (b) for experiments with (solid) and without (dashed) radiation.

Another two experiments have been made under conditions without the inclusion of turbulence, but with and without the incorporation of radiation. Only very small differences in both IWC and latent heat are found in these two experiments. This is due to the fact that radiation itself cannot play a significant role in the net ice formation in the ice generation region nor in the net sublimation of ice to water vapor in the lower region. Likewise, if radiation is not included, turbulence cannot produce larger differences in IWC, as shown in Fig. 4.

In summary, the simulation results in terms of a number of physical parameters denoted above are sensitive to turbulent and the radiative processes. Turbulence directly affects ice microphysics by producing higher supersaturation. Also, it can influence radiation by enhancing the net cooling rate and reducing the radiative stabilization. The interactions among radiation, turbulence and microphysics play an important role in the life cycle of cirrus clouds.

5. CONCLUSIONS

A two-dimensional numerical model has been developed to investigate the interactions among radiative processes, turbulence, and ice microphysics and their effects on the formation of cirrus clouds. A second-order 4-level turbulence closure model has been developed and incorporated into the present model. An advanced radiative scheme is used to account for the radiative processes. Sublimation between water vapor and ice water as well as the fall speed of ice water have been accounted for based on parameterizations.

Cirrus clouds are first formed by the dynamic and thermodynamic forcings. Once a sufficient amount of ice water is produced in the atmosphere, radiative processes begin to play an important role through its net cooling effect on the cloud top. The induced turbulence has significant effects on the phase changes and the ice water

formation. Also, turbulence affects the radiative processes by increasing the net radiative cooling in the ice water generation region, which is important in the maintenance of cirrus clouds.

Acknowledgments. Research work reported in this paper has been supported by the Air Force Office of Scientific Research under Grant F49820-94-1-0142.

REFERENCES

- Arakawa, A., 1966: Computational design for long-term numerical integration of the equations of fluid motion: Two dimensional incompressible flow. Part I. *J. Comput. Phys.*, 1, 119-143.
- Blackadar, 1962: The vertical distribution of wind and turbulence exchange in neutral atmosphere. *J. Geophys. Res.*, 67, 3095-3102.
- Curry, J. A., 1985: Interactions among turbulence, radiation and microphysics in Arctic Stratus clouds. *J. Atmos. Sci.*, 43, 90-106.
- Fu, Q., and K. N. Liou, 1992: On the correlated k-distribution method for radiative transfer in nonhomogeneous atmosphere. *J. Atmos. Sci.*, 49, 2139-2156.
- Fu, Q., and K. N. Liou, 1993: Parameterization of the radiative properties of cirrus clouds. *J. Atmos. Sci.*, 50, 2008-2025.
- Heymsfield, A. J., 1975: Cirrus uncinus generating cells and the evolution of cirriform clouds. Part I: Air craft observations of the growth of the ice phase. *J. Atmos. Sci.*, 32, 799-808.
- Heymsfield, A. J., and R.M. Sabin, 1989: Cirrus crystal nucleation by homogeneous freezing of solution droplets. *J. Atmos. Sci.*, 46, 2252-2264.
- Jensen, E. J., O. B. Toon, D. L. Westphal, S. Kinne, and A. J. Heymsfield, 1994: Microphysical modeling of cirrus: 1. Comparison with 1986 FIRE IFO Measurements. 2. Sensitivity studies. *J. Geophys. Res.*, 99, 10421-10454.
- Lilly, D. K., 1965: On the computational stability of numerical solutions of time-dependent nonlinear geophysical fluid dynamics problems. *Mon. Wea. Rev.*, 9, 11-26.
- Liou, K. N., Q. Fu, and T. P. Ackerman, 1988: A simple formulation of the δ -four-stream approximation for radiative transfer parameterizations. *J. Atmos. Sci.*, 45, 1940-1947.
- Liou, K. N., 1992: *Radiation and Cloud Processes in the Atmosphere: Theory, Observation, and Modeling*. Oxford University Press, New York, 487pp.
- Mellor, G. L., and T. Yamada, 1974: A hierarchy of turbulence closure models for planetary boundary layer. *J. Atmos. Sci.*, 31, 1791-1806.
- Starr, D. O'C., and S. K. Cox, 1985: Cirrus clouds. Part I: Cirrus cloud model. *J. Atmos. Sci.*, 42, 2663-2681.
- Takano, Y. and K. N. Liou, 1989: Solar radiative transfer in cirrus clouds. Part I: Single-scattering and optical properties of hexagonal ice crystals. *J. Atmos. Sci.*, 46, 3-19.

13.1 OBSERVATIONS OF CIRRUS CLOUD EXTENT AND THEIR IMPACTS TO CLIMATE

D. Frankel*, K.N. Liou, S.C. Ou
Department of Meteorology/CARSS
University of Utah
Salt Lake City, Utah

D.P. Wylie, and P. Menzel
University of Wisconsin
Madison, Wisconsin

1. INTRODUCTION

In a period of history when jet aircraft dominate the skies, questions arise as to the impact of such activity on the atmosphere. Machta and Carpenter (1971) and Liou *et al* (1990), showed that there was an increase in the amount of high cloud cover between 1948 to 1984 when lower clouds were not present at various sites over the United States. They further suggested that a correlation existed between this increase in high cloud cover and increases in jet traffic. More recently, the formation and effect of contrail clouds arising from jet engine exhaust plumes has received considerable attention. Contrail clouds trap outgoing longwave radiation emitted from the earth and the troposphere and keep the surface warm, referred to as the greenhouse effect. At the same time, these clouds reflect incoming solar radiation and reduce the solar energy available to the surface, referred to as the solar albedo effect. The balance between these two effects determines the tendency of the surface temperature change. Various studies have shown that cirrus and contrail cirrus tend to have its greenhouse effect dominating the solar albedo effect, therefore causing a net warming at the surface (Manabe 1975, Freeman and Liou 1979, Sinha and Shine 1974, Liou 1986).

A significant increase in jet fuel consumption in the 1960's corresponding to an increase in cirrus cloud cover has been documented. While for the current study an accurate figure of jet fuel consumption over the local areas of cloud data analysis is not available, extensive studies on global jet fuel consumption and air traffic patterns and populations have been undertaken. Jet fuel consumption statistics and projections between 1978-2000 showing continual increases (Nusser and Schmitt 1990), which implies increased tropospheric water vapor emissions. While contrail formation is a subject requiring considerable research, it is clearly related to water vapor concentration. This could be one reason that as jet

traffic appears to be increasing, so does cirrus cloud extent. Consequently, a correlation between jet air traffic and cirrus cloud cover becomes a tool in assessing the climatic impact of the former.

Contrails tend to form in the vicinity of the tropopause. In this is the region the ambient temperature allows supersaturated water vapor emitted from jet engines to quickly go into ice phase. Residency times for particles may vary from days below the tropopause up to a year above the tropopause in the lower stratosphere (Grassl 1990). As the ambient water vapor mixing ratio is low in the upper troposphere and lower stratosphere, a small amount of water vapor in the exhaust plume has a substantially greater impact at these altitudes than in the lower troposphere. Thus jet aircraft could be a major source of water vapor in this region of the atmosphere. Further analysis of air traffic patterns shows that in general cruising altitudes are within contrail cirrus producing levels. There are other considerations as well, the emission of SO_x and NO_x from jet engines could contribute to ice nucleation as well as have their own radiative effects. And even if the water vapor emitted does not form contrail cirrus it is the most important feedback process involved in greenhouse perturbations. Water vapor emission from jet engines is roughly proportional to jet fuel consumption (Nusser and Schmitt 1990), and projections indicate that global jet fuel consumption will continue to increase into the twenty first century.

2. CIRRUS CLOUD CLIMATOLOGY

While cirrus cloud data is not prevalent, this paper studies some of the existing climatologies. Cirrus cloud cover data was analyzed for the later twentieth century. The data is comprised of local surface observations over urban airports in the United States spanning forty years, and five years of satellite data taken from the HIRS radiometer on the NOAA polar orbiting satellite.

The surface observations of cloud covers include datasets for Salt Lake City, Chicago, Denver, and San Francisco. To be consistent with previous

Corresponding author address: Daniel E. Frankel, Univ. of Utah, Dept of Meteorology, Salt Lake City, Utah 84112 email : <dfrankel@climate.met.utah.edu>

cloud cover data sets (Machta and Carpenter 1971, Liou *et al.* 1990), cirrus data was only considered when the combined cloud cover of lower and middle clouds was less than or equal to 5%. This was held for all the surface observation data sets. Observations were taken hourly and from this data a daily average, monthly, and annual average cloud covers were calculated. Subject to the preceding conditions, all observed layers containing the cirrus types described below were summed to obtain the total cirrus cloud cover for that observation. It should be noted that this analysis would tend to underestimate cirrus covers due to overlap over underlying opaque low and middle cloud layers. The cirrus cloud cover statistics presented here considers various cloud types: cirrus, cirrostratus, cirrocumulus, and cirrocumulus standing lenticular.

Based on the analysis of domestic jet fuel consumption, significant increases occurred in about 1964 (Liou *et al.* 1990). Thus we study the cloud climatology for various midlatitude cities using this year as a reference year. Viewing the Salt Lake City observations, two populations of cloud data can be discerned, as illustrated in Figure 1(a). The first covers the dates between 1949-1964 and has an average values of 0.115. Then the cloud cover increases from 1964-1993 with an average of 0.202.

A linear fit is also made for the whole record to show the tendency. In effect we see a doubling of cloud cover over the time period of the entire data set. While cloud cover is variant under weather and temporary climate perturbations such as volcanic aerosol, the data shows a significant increase in annual average cloud cover as is indicated in the figure.

Another dataset of comparable time period was investigated. Chicago shows increased annual average values of cirrus cloud cover (Fig. 1(b)), though not as strong an increase as Salt Lake City perhaps due to the more saturated environment of the Chicago area.. The data set for Denver dates back to 1945 but no data is available for the 1970-1984 period. Significant differences in mean cloud cover are evident before and after about 1964, as shown in Fig 1(c). For San Francisco, data is available after 1985 and the cirrus cloud cover values are comparable to those for Salt Lake City and Denver. It should be noted that within a fifty year period the data is highly variable for all the cases and hence it is appropriate to examine the cloud cover tendencies.

Supplementing the surface observation cirrus cloud cover are datasets determined from the polar-orbiting High-Resolution Infrared Radiation Sounder (HIRS) on board NOAA satellites, over the time period from June 1989 to September 1995. The HIRS observations are based on the so called CO₂ slicing method which uses the multispectral channels in the 15 mm CO₂ band to retrieve cloud cover statistics (Wylie *et al.* 1994). Due to the method of detection, the cirrus classification is inherently different between

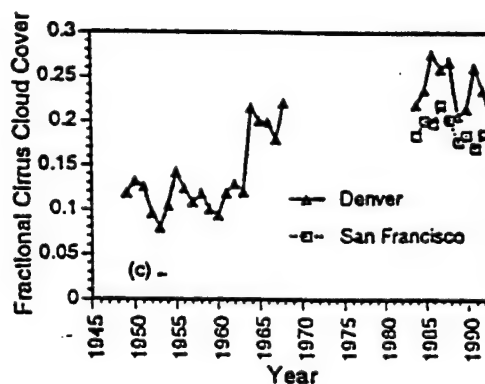
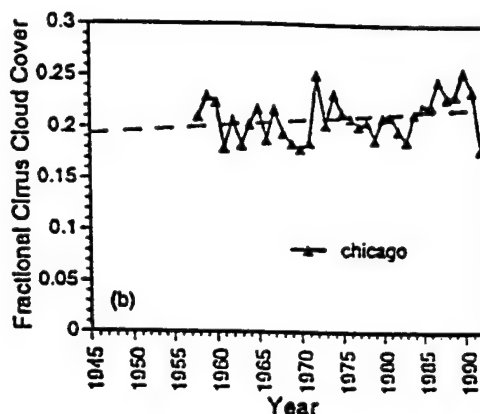
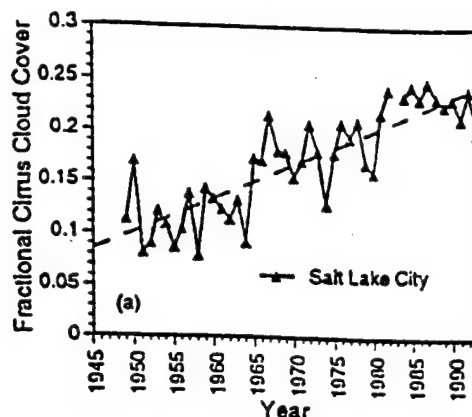


Figure 1. Cloud covers for respective cities.

surface and satellite observations. The HIRS data is expressed in terms of effective emissivity, which is an average emissivity measured over an approximately 20 km x 20 km field of view. For the HIRS observations to be considered cirrus the effective emissivity must be less than 0.95, corresponding to an optical depth less than 3.0. HIRS data shows cirrus clouds regardless of lower clouds. This will tend to make the HIRS cloud cover statistics have higher values than the surface observation statistics. The portion of HIRS data included in the present study covers the 65°S to 65°N geographical area. Poleward of this band was not considered, due to data availability. This dataset

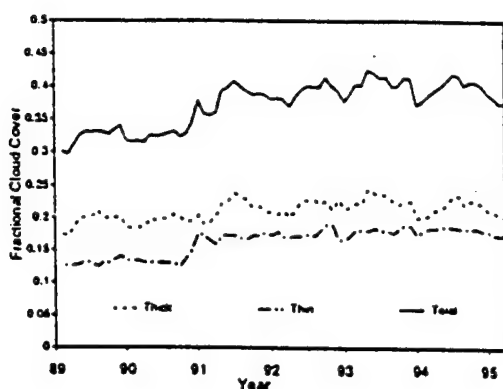


Figure 2. Cirrus cloud covers detected by HIRS.

includes cirrus in two categories; thin cirrus with effective emissivity of less than or equal to 0.5 (optical depth of 0.7 or smaller), and thick cirrus with effective emissivity of greater than 0.5 (optical depth greater than 0.7). The data was presented in the form of monthly averages in which measurements made over water and land were distinguished. For the purposes of this study the measurements over water were weighted 75% against the 25% over land to form a single average cirrus cover for each month.

Figure 2 shows the total, thick and thin cirrus covers detected by HIRS. In calculating the total cirrus cloud cover, the thin cirrus frequency was multiplied by 0.72, a statistical average of the effective emissivity, to obtain the cloud fraction. While significantly higher than surface observation data as discussed earlier, the HIRS data shows a global increasing trend over the four year period of June 1989 to September 1993. In June 1989 the value is 0.30. The cirrus cover increases over time to finish at an average of 0.40. Hence local surface observations taken over a long time scale and satellite observations taken over a large spatial scale but short time scale demonstrate a definite increase in cirrus cloud cover based on consistent satellite observations.

3. CLIMATIC IMPACT OF CIRRUS ON SURFACE TEMPERATURE

To consider the effects of global cirrus cover to climate, a one-dimensional radiative-convective model (Frankel 1995) was used to calculate temperature perturbations under a condition of changing cirrus cover over time. This model is designed to maintain global energy balance and progress to a state of thermal atmospheric equilibrium in the context of an annual and spatial averaged entity. This affords the opportunity to look at atmospheric cloud-radiation interactions in great detail and with a

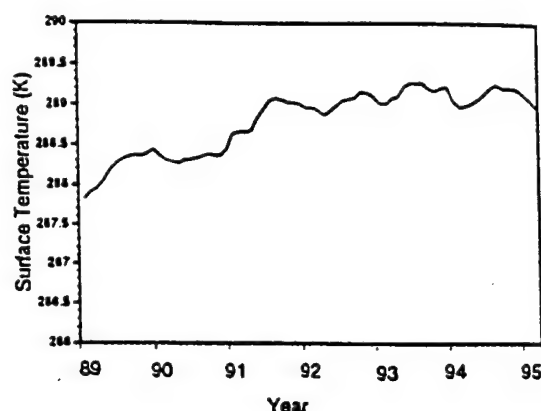


Figure 3. Surface temperatures from model output.

high vertical resolution. The model uses the radiative scheme of Fu and Liou (1993). The scheme consists of the delta-four stream method for the transfer of both solar and thermal infrared radiation in inhomogeneous atmospheres including clouds and the correlated k-distribution method to handle non-gray gaseous absorption in multiple scattering atmospheres. In particular, the scattering and absorption properties of hexagonal ice crystals were incorporated in the radiation scheme in terms of parameterization forms based on the unified theory of light scattering by ice crystals covering all sizes and shapes (Liou and Takano 1994, Yang and Liou 1996 a, b). The convective part of the model computes a convective adjustment and implicit convective flux similar to that found in traditional radiative-convective models (Manabe 1975). The model was tuned to the Standard Atmosphere with the total cirrus cloud cover fixed to a value corresponding to the first month of the HIRS data.

To assess the effects of the increase in total cirrus cover the 1-D model was run interactively using the HIRS results. Initialized to thermal equilibrium and a surface temperature of 288.07 K under the condition of cirrus cloud cover fixed to the value from June 1989 HIRS data, the model was then let to run for a number of timesteps equivalent to four years, updating the cloud cover in the model every month to a new HIRS value. The model output temperatures are shown in Fig. 3. A linear regression of this curve shows an increase of 1.2 K for a five year period. Liou, *et al* (1990) found for a 5% increase in contrail cirrus cover rendered a surface temperature increase of 1 K. The net cirrus increase in the HIRS dataset is approximately 10% fractional cloud cover, increasing from approximately 30% cover to 40% cover. The present result of 1.2 K temperature change appears to be consistent with other climate models. This is a substantial temperature perturbation, and suggests that without other influences, the increase of cirrus cloud cover could lead to produce a significant warming

effect.

Although the conditions under which jet aircraft contrails become cirrus clouds are not well understood at this point, both surface and satellite observations show that cirrus cloud cover appears to be on the increase. Thin cirrus clouds have a warming effect upon the lower troposphere through radiative forcing, and a numerical model study suggests that observable cirrus cloud cover increase would have a noticeable impact upon surface temperatures.

Acknowledgments. Research reported in this paper has been supported by NASA Grant NAG5-2678 and AFOSR Grant F49620-95-1-0376.

REFERENCES

- Frankel, D.E., 1995: Cirrus microphysical feedbacks as viewed through a one-dimensional radiative convective model. Thesis, Department of Meteorology, University of Utah.
- Freeman, K.P., and K.N. Liou, 1979: Climatic effects of cirrus clouds. *Adv. Geophys.*, **21**, Academic Press, 221-234.
- Fu, Q. and K.N. Liou, 1993: Parameterization of the radiative properties of cirrus clouds. *J. Atmos. Sci.*, **40**, 2008-2025.
- Grassl, H., 1990: Possible climatic effects of contrails and additional water vapour. *Air Traffic and the Environment- Background, Tendencies and Potential Global Atmospheric Effects* (U. Schumann, Ed.) Springer Verlag, 154-169.
- Liou, K.N. and Y. Takano, 1994: Light scattering by nonspherical particles: Remote sensing and climatic implications, *Atmos. Res.* **31**, 271-298.
- Liou, K.N., S.C. Ou, and G. Koenig, 1990: An investigation on the climatic effect of contrail cirrus. *Air Traffic and the Environment- Background, Tendencies and Potential Global Atmospheric Effects* (U. Schumann, Ed.) Springer Verlag, 154-169.
- Manabe, S., 1975: Cloudiness and the radiative convective equilibrium. *The Changing Global Environment* (S.F. Singer, Ed.), Reidel, 175-176.
- Nusser, H.-G., A. Schmitt, 1990: The global distribution of air traffic at high altitudes, related fuel consumption and trends. *Air Traffic and the Environment- Background, Tendencies and Potential Global Atmospheric Effects* (U. Schumann, Ed.) Springer Verlag, 154-169.
- Sinha, A., and K.P. Shine, 1994: A one-dimensional study of possible cirrus cloud feedbacks. *J. Climate.*, **7**, 158-173.
- Wylie, D.P., W.P. Menzel, H.M. Woolf, and K.I. Strabala, 1994: Four years of global cirrus cloud statistics using HIRS. *J. Climate.*, **7**, 1972-1986.
- Yang, P., and K.N. Liou, 1996 a: Finite-difference time domain method for light scattering by small ice crystals in three-dimensional space. *J. Opt. Soc. Am. A.*, **13**, 2072-2085.
- Yang, P., and K.N. Liou, 1996 b: A geometric-optics /integral-equation method for light scattering by non-spherical ice crystals. *Appl. Opt.* (November).

On the radiative properties of contrail cirrus

K. N. Liou¹, P. Yang¹, Y. Takano¹, K. Sassen², T. Charlock³, and W. Arnott⁴

Abstract. Using the observed ice crystal size distribution in contrail cirrus from SUCCESS, we have carried out the scattering and absorption calculations based on a unified theory for light scattering by ice crystals covering all sizes and shapes. We illustrate the effects of ice crystal size and surface roughness on the scattering phase function features for remote sensing applications. The extinction coefficient and single-scattering albedo exhibit a minimum feature at 2.85 μm , referred to as the Christiansen effect, which is particularly pronounced for clouds consisting of a significant number of small ice crystals. Based on a line-by-line equivalent solar model, we show from spectral curves that cloud reflection increases as ice crystal sizes become smaller, but the cloud absorption increase is only evident for wavelengths longer than about 2.7 μm . The ice crystal shape has a substantial effect on the cloud reflection and absorption for a given size; more complex ice particles reflect more solar radiation. Finally, we propose a contrail cirrus cloud model consisting of a combination of bullet rosettes (50%), hollow columns (30%), and plates (20%), with sizes ranging from 1 to 90 μm in association with radiation perturbation studies.

Introduction

One of the fundamental objectives of Subsonic Aircraft: Contrail and Cloud Effects Special Study (SUCCESS) is to provide the necessary and sufficient data to better determine the radiative properties of contrail cirrus and their potential impact on climate. Contrails tend to form in the vicinity of the tropopause in which the ambient temperature allows supersaturated water vapor emitted from jet engines to effectively convert into ice phase. Resident times for particles may vary from days below the tropopause and up to a year above the tropopause in the lower stratosphere. Analysis of air traffic patterns illustrates that, in general, cruising altitudes are within contrail cirrus producing levels. A number of statistical studies have indicated a significant correlation between jet fuel consumption and high cloud frequencies in urban airports [Liou et al., 1990; Frankel et al., 1997]. In particular, the data from Salt Lake City appear to support the connection between increasing jet aircraft operations in the upper troposphere, cirrus cloud cover, and regional climate when a sharp increase in domestic air traffic occurred in the mid-1980s.

Because of the lack of *in situ* microphysical observations in contrails, their radiative properties are largely unknown. The unique SUCCESS field experiment carried out over Kansas in April-May, 1996 provided mi-

crophysical measurements on the size and shape characteristics of ice crystals that were not available in the past. Using the observed ice crystal size distributions and shape factors for contrails, we have performed scattering and absorption calculations based on a unified theory for light scattering by ice crystals introduced in the text. Pertinent results for the extinction coefficient, single-scattering albedo, and phase function for contrail cirrus are presented. Employing a line-by-line equivalent solar model, we have also determined the spectral and broadband radiative properties of contrail cirrus.

Ice Crystal Size Distributions

During SUCCESS on May 4, 1996, ice crystal size distributions for the contrails were measured by the replicator system mounted on NASA's DC-8 that tailed a Boeing 757 by about 50 sec with aircraft separation distance of 11.5 km over northeast Oklahoma. This replicator system was developed by the scientists at the Desert Research Institute (DRI), University of Nevada [Arnott et al., 1994]. Two representative ice crystal size distributions, associated with the ambient temperature and dew point of -61.1°C and -62.9°C , respectively, were selected for the present study. The growth of ice crystals in the contrails took about 50 sec. The ice crystal images collected by the DRI replicator system show that they were predominately bullet rosettes, columns, and plates with sizes ranging from about 1 μm to about 90 μm .

In addition to the preceding data, we have also obtained two ice crystal size distributions from an experiment sponsored by the Department of Energy that was carried out over the Cloud and Radiation Testbed (CART) site located in Northern Oklahoma and Southern Kansas on April 18 and 19, 1994. On 18 April, a contrail was studied above the CART site when the University of North Dakota Citation aircraft re-penetrated its own contrail after 6 min of growth at a height of 13 km and a temperature of -85.9°C . As shown in Sassen [1997], the DRI replicator indicated minute, simple plate and column crystals in the contrail. The data for 19 April, on the other hand, came from near the top (13.4 km and -69.4°C) of an optically thin cirrostratus cloud with embedded contrails, which contained minute solid ice particles. Since this cloud generated a lunar corona display, as contrails frequently do, we consider this cloud composition as a proxy of a persisting contrail. The size distribution data were derived from the FSSP device, which has been shown to yield reliable data when appreciable numbers of ice crystals larger than 50–100 μm are not present [Gayet et al., 1996].

To characterize the effect of ice crystal size distributions on the radiative transfer results and to account for various shapes and sizes, we define the mean effective ice crystal size in terms of the maximum dimension, D , in the form

$$D_e = \int Vn(D)dD / \int An(D)dD = \frac{IWC/\rho_i}{A_e} \quad (1)$$

where V and A are the volume and projection area of an ice crystal, respectively, IWC is the ice water content,

¹Department of Atmospheric Sciences, University of California, Los Angeles, California.

²University of Utah, Salt Lake City, Utah.

³Langley Research Center/NASA, Hampton, Virginia.

⁴Desert Research Institute, Reno, Nevada.

LIU ET AL.: RADIATIVE PROPERTIES OF CONTRAIL CIRRUS

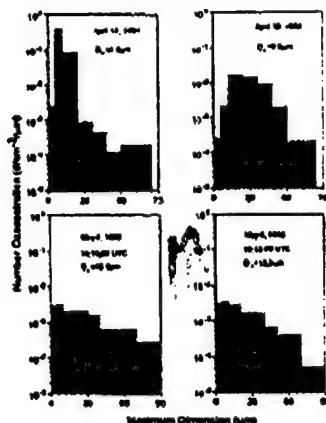


Figure 1. Discretized ice crystal size distributions for contrail cirrus (~ 50 sec duration) measured by the replicator system mounted on NASA's DC-8 that tailed a Boeing 757 during SUCCESS on May 4, 1996, and for a contrail and a cold cirrus (~ 6 min duration) measured by FSSP on board the University of North Dakota Citation on April 18 and 19, 1994 (upper panel).

ρ_i is the bulk ice density, and A_i is the projected area per unit volume. The mean effective ice crystal size so defined is now directly related to IWC , a prognostic parameter in GCMs. Also, by using the volume and projection area, the irregular ice crystal shape can be accounted for. Finally, A_i can be determined directly from the ice crystal images.

For single-scattering calculations, the observed ice crystal size distributions are discretized in eight bins: 1–5 μm with bin-center at 3 μm ; 5–10 μm with bin-center at 7.5 μm ; 10–20 μm with bin-center at 15 μm ; 20–30 μm with bin-center at 25 μm ; 30–40 μm with bin-center at 35 μm ; 50–70 μm with bin-center at 60 μm ; 70–90 μm with bin-center at 80 μm . Shown in Figure 1 are the discretized ice crystal size distributions. A substantial number of small ice crystals on the order of 10 μm is seen for the contrail that occurred on April 18, 1994.

Based on the SUCCESS replicator data, we estimate that contrails consist approximately of 50% bullet rosettes, 30% hollow columns, and 20% plates. Using these combinations, the mean effective sizes for the four ice crystal size distributions are 4.9, 9.8, 15.9, and 13.3 μm . The contrails observed on April 18 and 19 contain smaller ice particles than those observed on May 4.

Phase Function and Single-Scattering Properties

We have used the Monte-Carlo/geometric-ray-tracing approach to determine the scattering, absorption, and polarization properties of plates, solid and hollow column, dendrites, bullet rosettes, aggregates, and ice crystals with irregular surfaces whose sizes are much larger than the incident wavelength [Takano and Liou, 1995]. For light scattering by small ice crystals, we have innovated an improved geometric-ray-tracing method and a finite-difference time domain (FDTD) method [Yang and Liou, 1996a,b]. The improved model is applicable to size parameters as small as about 15. The FDTD method is a numerical technique for the solution of the Maxwell equations in time and space using appropriate absorbing boundary conditions. It is considered to be

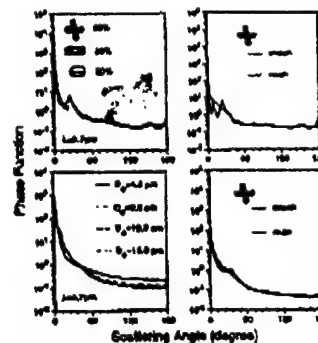


Figure 2. Phase functions for 0.7 and 3.7 μm wavelengths using a contrail cirrus model consisting of 50% bullet rosettes, 30% hollow columns, and 20% plates (left panel). The effect of ice crystal surface roughness on phase function is shown in the right panel using bullet rosette as an example.

the exact numerical solution for light scattering by particles, as verified by the exact theoretical solutions for long circular cylinders and spheres. Because of numerical round-off errors and required computer CPU time, the FDTD method can only be applied to ice crystal size parameters smaller than about 10–15. By unifying the modified geometric optics and EDTD methods for large and small size parameters, respectively, we are now in a position to determine the basic scattering, absorption, and polarization properties of ice crystals of any sizes and shapes that can be defined numerically.

The single-scattering parameters in terms of phase function, single-scattering albedo, and extinction cross section are computed for the solar spectrum covering 0.2 to 5 μm for about 200 wavelengths. The diagrams in the left panel in Figure 2 show the phase functions for the wavelengths of 0.7 and 3.7 μm . Substantial differences in the phase function for the four cases are noted at 3.7 μm at which ice is strongly absorptive and the ice crystal size has a significant impact on the single-scattering feature. For the case of 4/18/94, the halo peaks and backscattering for the 0.7 μm reduce substantially because of small ice crystal sizes.

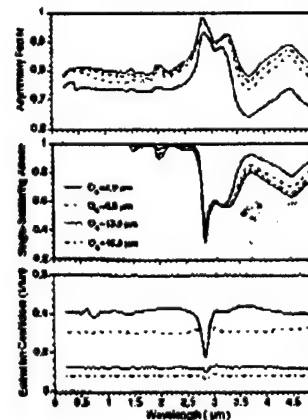


Figure 3. Asymmetry factor, single-scattering albedo, and extinction coefficient as functions of wavelength from 0.2 to 5 μm . The minima located at 2.85 μm are the well-known Christiansen effect.

LIU ET AL.: RADIATIVE PROPERTIES OF CONTRAIL CIRRUS

From the replicator data, it appears that some ice crystals may not be exactly hexagonal in shape and that some may have rough surfaces. Following Takano and Liou [1995], we have used a Monte-Carlo/geometric-ray-tracing approach to account for the Fresnelian interactions between rays and rough surfaces of an ice crystal defined by the first-order Gram Charlier Series distribution [Cox and Munk, 1954]. The diagrams in the right panel of Fig. 2 illustrate the phase function differences between smooth and rough surfaces using bullet rosettes as an example. The smooth-surface bullet rosettes produce halo peaks at 22° , 46° , and 10° , as well as the backscattering peak and a maximum feature at about 150° at $0.7 \mu\text{m}$. All of these peak features are smoothed out when the roughness on the surface is incorporated in the light scattering calculations. For strongly absorptive cases, the effect of surface roughness on the phase function for randomly oriented ice crystals is small because the scattering features are generated primarily by external reflections.

Figure 3 shows the asymmetry factor, single-scattering albedo, and extinction coefficient based on the shape model of 50% bullet rosettes, 30% hollow columns, and 20% plates. The extinction coefficients show little variation, except for a minimum in the $2.85 \mu\text{m}$ region, the so-called Christiansen effect. This effect occurs when the real part of the refractive index approaches 1 while the corresponding imaginary part is substantially larger, leading to the domination of absorption in light attenuation. It is particularly pronounced when ice particles are small, such as the 4/18/94 case. The single-scattering albedo also displays a strong minimum in the $2.85 \mu\text{m}$ region with values much less than 0.5. When absorption is substantial, the scattered energy is primarily contributed by diffraction in the forward directions. For this reason, maximum values of the asymmetry factor are noted around $3 \mu\text{m}$. Introducing the roughness of ice crystal surfaces does not significantly affect the extinction coefficient and single-scattering albedo patterns. It should also be noted that soot particles can be activated as ice nuclei in contrail formation and the effect on the scattering and absorption of ice particles is dependent on their relative sizes.

Spectral and Broadband Solar Albedos

We have developed a new solar radiation model with a high spectral resolution similar to line-by-line calculations in the thermal IR, hereafter referred to as the line-by-line equivalent (LBL) solar model. The spectral resolution has two options: 1 cm^{-1} with 10 g/s and 50 cm^{-1} with 30 g/s , where g denotes the cumulative probability function in the correlated k-distribution method. The correlated k-coefficients for these spectral intervals for H_2O from $2,000$ to $21,000 \text{ cm}^{-1}$ (0.5 – $5 \mu\text{m}$) are determined from the updated 1996 HITRAN data based on the method developed by Fu and Liou [1993]. The correlated k-coefficients for the 2.0 and $2.7 \mu\text{m}$ CO_2 bands are also derived, in which overlaps between H_2O and CO_2 lines are accounted for by means of the multiplication rule. Absorption due to O_3 and O_2 bands and Rayleigh scattering contributions are accounted for based on the conventional method. In addition to cloud particles, we have also compiled the single-scattering properties of six typical aerosol in connection with the LBL solar model.

The "exact" adding/doubling radiative transfer program including full Stokes parameters developed by Takano and Liou [1989] is used to calculate the transfer of monochromatic solar radiation in a vertically inhomogeneous atmosphere which is divided into 51 layers. For wavelengths between 3.7 to $5 \mu\text{m}$, thermal emission

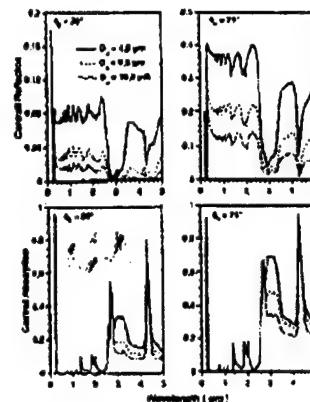


Figure 4. Spectral reflection and absorption for contrail cirrus as a function of the mean effective ice crystal size for two solar zenith angles. The contrail cirrus were located at 12 km over a land surface with a Lambertian albedo of 0.2 and with an IWP of 1 gm^{-3} .

contributions to the solar flux transfer are accounted for by adding the thermal emission part, $(1 - \bar{\omega})\pi B_\lambda(T)$, to the adding/doubling method, where $\bar{\omega}$ is the single-scattering albedo and $\pi B_\lambda(T)$ is the Planck flux for a given temperature. The thermal part, although small, has not been accounted for in broadband solar flux calculations and could be a noticeable energy source in the upper part of the atmosphere; a subject for future exploration. The spectral solar radiative transfer program also includes the options of using the detailed solar irradiance data averaged over appropriate spectral resolutions.

Figure 4 illustrates the spectral reflection and absorption for the contrail layer as a function of the mean effective ice crystal size for two solar zenith angles of 30° and 75° . To economize the computations, we have used the spectral version of 50 cm^{-1} containing 30 g/s . From observations, the contrails were located at about 12 km over a land surface which is assumed to have a Lambertian albedo of 0.2 . In the calculations, we have employed an ice water path (IWP) of 1 gm^{-2} . The visible optical depth for an ice crystal cloud can be expressed in terms of both IWP and ice crystal size in the form [Fu and Liou, 1993]

$$\tau_v = IWP(a + b/D_e), \quad (2)$$

where a and b are certain coefficients. Thus, for a given IWP , the cloud reflection is inversely proportional to the mean effective ice crystal size D_e , as illustrated in Fig. 4. The water vapor absorption bands located at 3.2 , 2.7 , 1.87 , 1.38 , 1.1 , 0.94 – 0.82 , and $0.72 \mu\text{m}$ are clearly shown, as is the $4.3 \mu\text{m}$ carbon dioxide band. The large reflection in the UV region is primarily produced by Rayleigh scattering. For the solar zenith angle of 75° , substantial reflection is evident for wavelengths shorter than about $2.5 \mu\text{m}$, particularly for smaller D_e . The effect of ice crystal size on cloud absorption appears only for wavelengths greater than $2.8 \mu\text{m}$, at which absorption due to ice particles becomes more significant than absorption due to water vapor and carbon dioxide.

The broadband reflection and absorption for contrail layers as a function of IWP are shown in Figure 5. The left and right panels illustrate the effects of ice crystal size and shape on the cloud radiative properties, respectively. In the calculations, we have used a solar zenith angle of 30° and a surface albedo of 0.2 . Other input

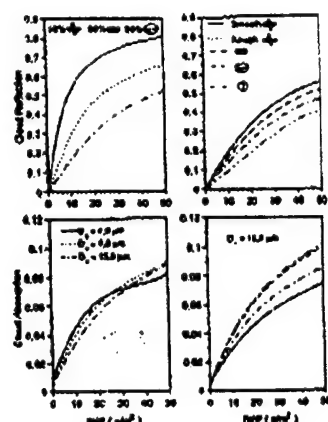


Figure 5. Broadband reflection and absorption for contrail cirrus as a function of IWP to illustrate the effects of ice crystal size (left panel) and shape (right panel). The solar zenith angle used is 30° .

parameters are the same. Cloud reflection for a given IWP is clearly dependent on ice crystal size: smaller ice crystals reflect more solar radiation than larger ice crystals. When IWP is smaller than about 20 gm^{-2} , cloud absorption also reduces when the ice crystal size increases. For IWP larger than about 20 gm^{-2} , cloud absorption for the case of $4.9 \mu\text{m}$ becomes the smallest because it is now determined by the single-scattering albedo rather than the optical depth. To investigate the shape effect, we have used a D_e of $15.9 \mu\text{m}$. The effect of roughness of bullet rosette surfaces on cloud reflection and absorption is insignificant. Cloud reflection values become progressively smaller for hollow columns, plates, and equal-area spheres because their asymmetry factors become increasingly larger to allow stronger forward scattering to occur. Cloud absorption values for plates, hollow columns, and equal-area spheres become larger because of the progressively smaller single-scattering albedo values.

Summary

We have analyzed two ice crystal size distributions for contrail cirrus collected during SUCCESS and obtained two additional distributions from an experiment that was carried out earlier over the DOE CART site. Using these four observed ice crystal size distributions, we have performed the scattering and absorption calculations to determine the single-scattering and phase function properties of ice particles that were present in contrails for wavelengths from 0.2 to $5 \mu\text{m}$. Based on the SUCCESS *in situ* observed data, we propose an ice crystal shape model for contrails consisting of 50% bullet rosettes, 30% hollow columns, and 20% plates in conjunction with radiation calculations.

For strongly absorptive cases, the ice crystal surface roughness is not a significant factor in determining the phase function pattern. The extinction coefficient shows a minimum feature at $2.85 \mu\text{m}$ referred to as the Christiansen effect, particularly pronounced when small ice crystals are present. The corresponding single-scattering albedo in this spectral region shows values much less than 0.5. Increasing the ice crystal size increases the asymmetry factor, whereas the reverse is true for the single-scattering albedo.

Based on a LBL solar model, the dependence of cloud reflection on the mean effective ice crystal size for a given IWP is clearly illustrated in the entire solar spectrum. For a given IWP , smaller ice crystals reflect more solar radiation than larger ice crystals. The

ice crystal shape has a substantial effect on the reflection and absorption calculations. For a given ice crystal size, cloud reflection values decrease progressively when bullet rosettes, hollow columns, plates, and equal-area spheres are employed in the calculations.

In order to investigate reliably the radiative and climatic effects of contrail cirrus, an appropriate ice crystal model in terms of size and shape is required. We have proposed a combination of bullet rosettes, hollow columns, and plates with sizes ranging from 1 to $90 \mu\text{m}$ for contrail cirrus in association with radiation perturbation studies. Finally, the subject of the finite and inhomogeneous nature of contrail cirrus on the radiative effects is one that requires further investigation.

Acknowledgments. This study was supported by NASA Grants NAG5-2678, NAG2-923, and NCC1-189, AFOSR Grant F49620-94-1-0142, and by the Department of Energy Grants DE-FG03-95ER61991 and DE-FG03-94ER61747.

References

- Arnott, W. P., Y. Y. Dong, and J. Hallett, Role of small ice crystals in radiative properties of cirrus: A case study, FIRE II, November 22, 1991, *J. Geophys. Res.*, **99**, 1371-1381, 1994.
- Cox, C., and W. Munk, Measurement of the roughness of the sea surface from photographs of the sun's glitter, *J. Opt. Soc. Am.*, **44**, 838-850, 1954.
- Frankel, D., K. N. Liou, S. C. Ou, D. P. Wylie, and P. Menzel, Observations of cirrus cloud extent and their impacts to climate, *Proceedings for the Ninth Conference on Atmospheric Radiation*, Am. Meteor. Soc., February 2-7, 1997, Long Beach, CA, 414-417, 1997.
- Fu, Q., and K. N. Liou, Parameterization of the radiative properties of cirrus clouds, *J. Atmos. Sci.*, **50**, 2008-2025, 1993.
- Gayet, J.-F., G. Febvre, and P. Larson, The reliability of the FMS FSSP in the presence of small ice crystals, *J. Atmos. Ocean. Tech.*, **13**, 100-1310, 1996.
- Liou, K. N., S. C. Ou, and G. Koenig, An investigation on the climatic effect of contrail cirrus, in *Air Traffic and the Environment Background, Tendencies and Potential Global Atmospheric Effects*, edited by U. Schumann, pp. 154-169, Springer Verlag, 1990.
- Sassen, K., Contrail-cirrus and their potential for regional climate change, *Bull. Amer. Meteor. Soc.*, **78**, 1885-1903, 1997.
- Takano, Y., and K. N. Liou, Solar radiative transfer in cirrus clouds. II: Theory and computation of multiple scattering in an anisotropic medium, *J. Atmos. Sci.*, **46**, 20-38, 1989.
- Takano, Y., and K. N. Liou, Radiative transfer in cirrus clouds. III: Light scattering by irregular ice crystals, *J. Atmos. Sci.*, **52**, 818-837, 1995.
- Yang, P., and K. N. Liou, Finite-difference time domain method for light scattering by small ice crystals in three-dimensional space, *J. Opt. Soc. Am. A*, **13**, 2072-2085, 1996a.
- Yang, P., and K. N. Liou, Geometric-optics-integral-equation method for light scattering by nonspherical ice crystals, *Appl. Opt.*, **35**, 6568-6584, 1996b.

K. N. Liou, P. Yang, and Y. Takano, Department of Atmospheric Sciences, UCLA, Los Angeles, CA 90095-1565

K. Sassen, Department of Meteorology, University of Utah, Salt Lake City, UT 84112

T. P. Charlock, Atmospheric Sciences Division, Langley Research Center/NASA, Hampton, VA 23665

W. P. Arnott, Atmospheric Sciences Center, Desert Research Institute, Reno, NV 89506

(Received July 10, 1997; revised November 20, 1997; accepted November 25, 1997.)

AIRBORNE RETRIEVAL OF CIRRUS CLOUD OPTICAL AND
MICROPHYSICAL PROPERTIES USING ARES
5.1-5.3 AND 3.7 μm CHANNEL DATA

S. C. Ou, K. N. Liou, P. Yang, and P. Rolland
Department of Atmospheric Sciences, UCLA
Los Angeles, California

T. R. Caudill
Air Force Research Laboratory/VSBE
Hanscom AFB, Massachusetts

J. Lisowski
SCITEC, Princeton, New Jersey

B. Morrison
Aeromet, Inc., Tulsa, Oklahoma

Abstract

We present an airborne retrieval algorithm to infer cirrus cloud temperature, optical depth and mean effective sizes using the Airborne Remote Earth Sensing System (ARES) 5.1-5.3 and 3.7 μm channels data. The algorithm development and the selection of the channels are based on the principle and parameterization of radiative transfer involving cirrus clouds and the associated atmospheric and surface properties. It has been applied to the ARES data collected over the western Boston area on September 16, 1995. Validation of the retrieved parameters was carried out using the collocated and coincident ground-based 8.6-mm radar data and ice crystal size distribution measurements obtained from the 2D-P probe on board the High Altitude Reconnaissance Platform (HARP). We show that the retrieved cirrus cloud temperature, mean effective ice crystal size, and optical depth match closely with those derived from the observations.

1. Introduction

Established cirrus cloud retrieval methods based on imaging radiometric data generally use the visible, window (e.g., 3.7, 10.9, and 12.0 μm), and water vapor absorption (6.3 μm) channel radiances that are available from either operational satellites or research aircraft (Liou *et al.* 1990; Minnis *et al.* 1990, 1993; Baum *et al.* 1994; Ou *et al.* 1993, 1995). Remote sensing of the cirrus cloud parameters using radiances from other spectral channels has also been recently explored. Wielicki *et al.* (1993) investigated the possibility of using the 0.83 and 1.65 μm radiances from Landsat to determine ice crystal particle sizes. Gao and Kaufman (1995) reported a new technique for detecting thin cirrus clouds using the 1.38 and 1.88 μm water vapor absorption channels radiances from the Airborne Visible Infrared Imaging Spectrometer (AVIRIS), based on the fact that the low-level water vapor absorption provides a dark background for the high-altitude cirrus reflection to be detectable. The 1.6 and 2.2 μm channel radiances from the Moderate Resolution Imaging Spectrometer (MODIS) and the MODIS Airborne Simulator (MAS) are also potentially useful channels for future developments of cirrus cloud retrieval algorithms (King *et al.* 1992, 1995; Tsay *et al.* 1996), because both wavelengths are sensitive to variations in ice crystal size distributions. Moreover, the selection of appropriate channels for reliable cirrus cloud detection and retrieval will be a major consideration in the development of the National Polar-orbiting Operational Environmental Satellite System (NPOESS) project.

In this paper, we present an airborne retrieval algorithm to infer cirrus cloud temperature, optical depth, and ice crystal mean effective size using the ARES IR spectrometer data. The retrieval method utilizes for the first time the 5.1-5.3 μm water vapor band to determine cirrus cloud temperatures and IR emissivities, from which the associated optical depths can be determined from radiative transfer parameterizations. In the scheme, the ice crystal mean effective size is derived by matching the sum of the computed 3.7 μm solar reflected and IR emitted radiances with the ARES Ch. 42 (3.755 μm) radiances. The selection of these retrieval channels is based on the examination of the computed weighting functions of a typical midlatitude summer atmosphere along with the inspection of ARES channel radiance images. We have applied the retrieval algorithm to the ARES data collected during a mission flight, which was carried out on board the WB-57F aircraft on September 16, 1995 over the

western Boston area. The retrieved cloud parameters are compared with the *in-situ* 2D-probe measurements obtained from the Aeromet's HARP, as well as the cloud heights derived from the ground-based 8.6-mm radar returns.

Cloudy radiances have been measured by the IR imaging spectrometer/radiometer on board the ARES Programs' WB-57F high-altitude research aircraft operated by the NASA Johnson Space Flight Center. The WB-57F is capable of reaching altitudes in excess of 60,000 ft, and carries a crew of two, permitting instrument operation by a dedicated flight crew. The sensor was mounted on the lower fuselage surface, with downward viewing while in level flight. The ARES sensor for the present study has been operated as a 75-channel imaging spectrometer. It is operated in a pushbroom mode with 45-pixel array pointing in the nadir direction taking data at the standard rates of 10, 20, 40, or 80 scans/sec. The optical elements of ARES provide a pixel IFOV (instantaneous field of view) of slightly more than 1 mrad, which corresponds to about 15 m ground resolution for a flight altitude of 15 km. The spacing of the ARES spectral wavelengths appears to depend on the optical arrangement with the channel band widths that vary between 0.02 and 0.07 μm . Further details of the ARES can be obtained from the internet web site : <http://cahill.plh.af.mil:8600/PDAC.html>.

For validation of the retrieved cloud temperature/height, we have obtained the cloud boundary height data from the collocated and coincident ground-based 8.6-mm TPQ-11 radar measurements. For comparison of the retrieved cloud optical depth and mean effective sizes with *in-situ* measurements, we have also acquired the meteorological and ice microphysical data collected from the HARP, which is a Learjet 36A, flying in conjunction with the ground-based radar and the ARES measurements. The HARP carried instruments for taking both *in-situ* and remote atmospheric measurements. The *in-situ* instruments include Forward Scattering Spectrometer Probe (FSSP), 1D-C and 2D-C probes for particle size distribution measurements. Ambient temperatures were measured by the Rosemount Total Temperature Sensor with an uncertainty of ± 1 K.

This paper is organized as follows. In Section 2, we describe the development of the remote sensing algorithm for the retrieval of cirrus cloud temperature (height), optical depth, and ice crystal size principally using the ARES 5.1-5.3 and 3.7 μm channels. In Section 3, results of the application of this

retrieval scheme to the ARES data collected during September 16, 1995, are presented along with the validation efforts using the ground-based radar and airborne *in-situ* measurements. Finally, a summary is given in Section 4.

2. Principle of Retrieving Cirrus Parameters Using ARES Thermal IR Channels

The present retrieval method for inferring cirrus temperature and emissivity is based on the numerical solution of the following set of algebraic equations (Liou *et al.* 1990; Ou *et al.* 1993, 1995) :

$$R_i = (1 - \epsilon_i) R_{ai} + \epsilon_i B_i(T_c), \quad (1)$$

$$\epsilon_i = 1 - \exp(-k_i \tau), \quad (2)$$

where R_i is the upwelling radiances at the top of the cirrus cloudy atmosphere for the i th selected ARES channel; R_{ai} is the corresponding radiances reaching the cloud base for the i th channel; ϵ_i is the cloud IR emissivities, T_c is the mean cirrus temperature; $B_i(T_c)$ is the Planck intensities at T_c , τ is the visible optical depth and k_i is the effective extinction coefficient that has been determined from the calculated single-scattering properties based on a number of measured ice crystal size distributions. The behavior of the cloud emissivity in terms of its dependence on wavelength and cloud parameters has been examined previously (Liou *et al.* 1990).

By straightforward algebraic analyses, Eqs. (1) and (2) for a pair of channels ($i=1$ and 2) can be combined into a single equation in the form

$$[R_2 - B_2(T_c)] / [R_{a2} - B_2(T_c)] = \{ [R_1 - B_1(T_c)] / [R_{a1} - B_1(T_c)] \}^{k_2/k_1} \quad (3)$$

If R_{a1} and R_{a2} are known, $B_2(T_c)$ and $B_1(T_c)$ are approximately linearly correlated, and $k_2/k_1 \sim 1.0$, then Eq. (3) becomes a linear equation, whose numerical solution can be obtained in a relatively straightforward manner.

The effective extinction coefficients for the retrieval channels have been computed using the adding/doubling program in conjunction with the development of this remote sensing algorithm. Eleven ice crystal size distributions from aircraft *in-situ* measurements have been chosen (Fu and Liou 1993).

Their mean effective ice crystal sizes range between 23.9 and 123.6 μm . The single-scattering properties including phase functions, single scattering albedos, and extinction coefficients have been computed for each size distribution and for each of the selected ARES channels using the unified theory for light scattering by ice crystals (Yang and Liou 1996a, b). To optimize the computational effort, the forward-scattering peak of each phase function was truncated following the procedure developed by Takano and Liou (1989). Radiances for each channel and for a range of optical depths and ice crystal sizes were computed using the aforementioned adding/doubling program. The cirrus cloud emissivity, which is defined as the ratio of the upwelling radiance to the cloud Planck function, was obtained as functions of the optical depth, mean effective size, and channel wavelengths. Finally, the effective extinction coefficients for each channel and for each size distribution was obtained as the slope of the linear curve fitting of $-\ln(1-\epsilon_i)$ vs. τ . Figure 1 shows the effective extinction coefficient (k -value) as a function of the mean effective size for eight wavelengths. For all wavelengths, the k -values increase with the mean effective size. This functional dependence of the k -values has been incorporated into the retrieval program. More importantly, the diagram indicates that the values of the three pairs of k -ratios -- $k(5.189 \mu\text{m})/k(5.116 \mu\text{m})$, $k(5.261 \mu\text{m})/k(5.116 \mu\text{m})$, and $k(5.332 \mu\text{m})/k(5.116 \mu\text{m})$ —depend weakly on the mean effective size and are all close to 1.0 for the range of the mean effective size considered here. Thus, they are fixed at 1.0 in the numerical solution of Eq. (3).

In order to infer the cirrus emissivity, ϵ_i , and temperature, T_c , from multiple radiance measurements in cloudy conditions, the upwelling radiances at the cloud base, R_{ai} , must be known. In principle, it can be generated from forward radiation transfer calculations if the surface temperature, atmospheric temperature and humidity profiles, and cloud base height are given. However, a more direct and reliable method to determine R_{ai} would be to find clear column radiances from the available data.

Assuming that the water vapor absorption/emission effects are negligible above cirrus clouds, we may approximate the cloud-base upwelling radiance using the measured clear radiance at the ARES flight level. This approximation has been applied to the retrieval of cirrus cloud parameters using the AVHRR

3.7 and 10.9 μm window bands (Ou *et al.* 1993) and to the airborne cirrus retrieval using the 6.5 and 10.5 μm radiometer data (Liou *et al.* 1990). Once R_{ai} is determined, Eq. (3) can be solved by a numerical iteration method. Since there are two independent parameters, $N-1$ pairs of the $N (\geq 1)$ channel data are used in the retrieval program. $N-1$ sets of the retrieved temperature and emissivity are then averaged to obtain their respective mean values.

Upon retrieval of the IR emissivity and the cloud temperature using the thermal IR channels, we can obtain the mean effective size using the observed 3.7 μm channel radiances. We first assume a trial ice crystal size, from which the visible optical depth can be obtained from Eq. (2). The 3.7 μm thermal IR radiance can be calculated according to Eq. (1). The cloud-base upwelling 3.7 μm IR radiance can be obtained by converting the 4.75 μm clear-pixel radiance into its equivalent Planck function at 3.7 μm , since both channels are in the window spectral interval. The 3.7 μm solar reflectance is determined from look-up tables, which contains the computed value of the 3.7 μm solar reflectance as functions of the visible optical depth and the mean effective size. These tables are generated for the same six size distributions as described in Rao *et al.* (1995) and for appropriate solar-viewing geometries, using the adding/doubling method developed by Takano and Liou (1989). Finally, the total 3.7 μm radiance is calculated as the sum of the thermal IR and solar radiances. The radiance values thus obtained are subsequently compared with the observed 3.7 μm radiances. The mean effective ice crystal size can then be obtained iteratively by adjusting the trial value based on the difference between the computed and observed radiances. Pixels having a retrieved mean effective size greater than 123.6 μm or less than 23.9 μm are discarded. Figure 2 gives a schematic flow diagram for the retrieval of cirrus cloud temperature, emissivity (optical depth) and mean ice crystal size.

3. Application of the Retrieval Scheme to the ARES Spectrometer Data

The preceding cirrus cloud retrieval scheme is applied to the ARES spectrometer data obtained during the WB-57F flight that was conducted on September 16, 1995. The flight has been divided into eight tracks. Data collected for Tracks 1, 3, 5, and 8 were analyzed. These four tracks are straight, and

spectrometer data were recorded in nadir-pointing pushbroom mode. The flight time for each track is: 2055-2100 UTC (Track 1), 2135-2140 UTC (Track 3), 2212-2217 UTC (Track 5), and 2308-2313 UTC (Track 8). The cruise portion of each track was at an altitude of 15 km along the southeast-northwest direction, crossing over the Hanscom Air Force Base at Bedford, Mass., where the ground-based 8.6-mm radar was located. During the period of Tracks 1 and 3, HARP was also flying at the cirrus cloud level below the WB-57F. Between 2030 and 2040 UTC (case 1), and between 2147 and 2157 UTC (case 2), HARP flew in a race track pattern which was no more than 30 km from the Hanscom Air Force Base. Its flight tracks are approximately collocated and coincident with the route of the ARES Tracks 1 and 3, respectively. For both cases, the flight altitude was at about 8 km, close to the top of the cirrus cloud vertical domain.

3.1 ARES Channel Spectral Properties

Implementation of the preceding retrieval scheme requires understanding of the ARES channel spectral properties and the appropriate selection of useful ARES channel data. Figure 3 presents the upwelling radiances associated with solar reflection and thermal IR emission in the 2-6.4 μm region to assess the relative importance of the two radiation sources. For the solar reflection, we have used the updated solar irradiance data provided for our use by G. Anderson at the Air Force Geophysics Directorate (Anderson 1995). The results are shown for the cosine of two solar zenith angles and for a surface reflectance of 0.1. For the thermal IR emission, Planck function curves for three temperatures covering the range of relevant earth's atmospheres are shown. It is clear that for $\lambda < 3 \mu\text{m}$, the solar reflection is the primary contributor to radiation, while for $\lambda > 4.5 \mu\text{m}$, the thermal IR emission is the predominant radiation source. For $3 \mu\text{m} < \lambda < 4.5 \mu\text{m}$, the relative importance of the solar reflection and thermal IR emission depends on the sun's position, the surface albedo, and the atmospheric thermodynamic state. For the radiative transfer simulation and the remote sensing algorithm development, both components must be accounted for in this intermediate spectral range.

Based on the theory of atmospheric gaseous absorption, several absorption bands exist in the 2-6.4 μm spectral interval (Goody and Yung 1989). These include the 2.7 μm H_2O band produced by ν_1 and ν_2 fundamentals, the 3.2 μm H_2O band associated with $2\nu_2$, the 4.3 μm CO_2 band due to the ν_3 fundamental and P and R branches, and the H_2O 6.3 μm vibrational (ν_2)-rotational band. There are three windows located at the 2.2, 3.7, and 4.7 μm regions. Figure 4 shows typical ARES 75-channel spectra obtained over clear and cirrus cloudy areas. Respective spectral intervals for the absorption bands are noted in the diagram. Large measurement noises exist for Chs. 1-25 (1.9-2.7 μm), where the solar reflection contributions are dominant, and the cloud reflection is stronger than the surface reflection. For Chs. 26-75, the aforementioned four absorption bands and two window bands are clearly displayed as local minima and maxima within both spectra, respectively. Over the 3.7 μm and 4.7 μm window bands and the 6.3 μm water vapor absorption band-wing interval, there are significant differences between the clear and cloudy radiances. These differences can be used to detect the presence of cirrus clouds and to retrieve their optical and microphysical parameters.

3.2 Selection of Retrieval Channels

To select a number of appropriate channels for the cirrus cloud retrieval, we have examined all the ARES channel weighting function profiles and images. Typical weighting function profiles were generated using the vertical transmittance functions obtained from the MODTRAN calculations employing the climatological midlatitude summer temperature and humidity soundings. These weighting function profiles show features that correspond to the distribution of absorption bands. For the window channels (3.75 μm , and 4.7 μm), the weighting function peaks at or near the surface, so that the clear radiance is dominated by surface emission. The inhomogeneity of surface types and emissivity can cause clear radiance to spread, leading to errors in cloud retrieval results. For the 2.7 μm H_2O , 4.3 μm CO_2 , and 6.3 μm H_2O band-center channels, the weighting function peaks in the upper atmosphere. The radiance tends to be dominated by gaseous emission from the upper atmosphere, suppressing the cloud signals. For the 6.3 μm band-wing channels, the weighting function peaks in the middle and lower

troposphere. For the purpose of the detection and retrieval of cirrus clouds, it is advantageous to choose channels with the weighting functions peaking in the lower troposphere. This is because the data spread in clear radiance is reduced due to the relatively homogeneous and moderate water vapor emission in the band-wing spectral interval, and the upwelling emission of cirrus clouds can be unambiguously detected by satellite radiometers without attenuation by water absorption/emission in the upper atmosphere.

Moreover, we have used radiance images to facilitate the selection of channels by acquiring the ARES data collected on September 16, 1995 (No.16-9-95-1A). Using a quick-look software ADAPT (ARES Data Analysis and Processing Toolkit developed by the SCITEC Inc. at Princeton, N.J.), we can display graphically the large volume of the ARES dataset on a SGI system in imagery forms. We have manually examined the image of each flight track for each ARES channel, and have selected a scene which displays a distinct contrast between high- and low- radiance areas using the 4.747 μm channel imagery. Based on both ground-based 8.6 mm radar and airborne K_a -band radar and 0.53 μm lidar observations on board HARP, only a single layer of cirrus cloud was present during the flight period. Thus, the high- and low-radiance areas correspond to clear and cloudy regions, respectively. Figure 5 shows the radiance images for Chs. 41(3.681 μm), 42(3.755 μm), 55(4.747 μm), 60(5.116 μm), and 63(5.332 μm) over the selected scene. The first three channels are within the 3.75 μm and 4.7 μm window bands, while the last two channels are within the 6.3 μm water vapor band-wing interval. For each image, the horizontal and vertical scales are ~ 500 m and 2.5 km, respectively.

From these images, it is noted that the upper 1/3 of the domain is clear, while the rest of the domain is cloudy. Over the clear area, the images for the three window channels show significant variations of the emitted/reflected radiances due to the inhomogeneity of the surface temperature and emissivity. However, for the two band-wing channels, radiances over the clear area appear to be relatively uniform, as compared to the clear radiances for the window channels, because the significant water vapor absorption/emission effect in the lower troposphere covers the horizontally inhomogeneous surface emission. The narrow distribution of the clear radiances is a desirable feature for application of

the remote sensing algorithm. A smaller spread in clear radiances would lead to less errors in prescribing the mean clear radiances, thus increasing the retrieval accuracy (Rao *et al.* 1995).

Over the cloudy area, it is evident that the image for the 4.7 μm channel, as well as the images for the two band-wing channels, contain distinct cloud signatures. For the two 3.7 μm window channels, there is no distinguishable cloud signature, because the compensating effects of the strong reflection and weak emission by cloud particles cause the resulting total cloud radiance to be about the same as the total clear radiance. Radiance images for channels at the absorption band center (not shown here) exhibit no cloud signature. Based on the preceding discussions on the properties of the computed weighting function profiles and the images shown in Figure 5, we select Ch. 60, 61 (5.189 μm), 62 (5.261 μm) and 63 for the development of a cirrus cloud retrieval algorithm. The weighting function for these channels peaks in the lower troposphere, and images for these channels contain definitive cloud signatures and display narrow data spread of clear radiances.

3.3 Retrievals using ARES Channel Data

In order to apply the aforementioned algorithm to the inference of the cloud temperature and emissivity, we must first determine clear or cloudy pixels within any selected scene. Thus, we have developed a clear/cloud detection scheme to identify clear and cloudy data points. It is based on the physical properties of the ARES equivalent brightness temperatures for selected channels for clear and cloudy pixels. In this scheme, clear pixels are separated from the cloudy pixels by applying the threshold tests to the equivalent brightness temperature data for each selected channels. If the equivalent brightness temperature for a pixel is greater than the prescribed threshold value for each selected channels, then it is categorized as clear. Otherwise, it is flagged as cloudy. The resulting number of cloudy pixels may be overestimated in this scheme. However, by doing so, we can ascertain that the detected clear pixels have the maximum probability to be truly clear, and that the maximum amount of cloudy pixels are available for the retrieval to be carried out.

Appropriate threshold values for the selected channels are determined from statistical analyses on the radiance data for the particular case of the mission flight on September 16, 1995. Figures 6(a)-(d) show the histograms of the brightness temperatures for Chs 60-63 within the domain of Figure 5. Each histogram displays a distinct bi-modal shape due to the presence of contrasting clear and cloudy areas within the selected scene. As discussed previously, the high- and low-radiance modes represent the mean radiances for the clear and cloudy conditions, respectively. From these analyses, the threshold value for each channel can be easily determined as the radiance that is associated with the minimum frequency between the two modes. Once the clear pixels are defined, the mean clear radiance for each channel is determined based on the average of radiances of all detected clear pixels within the selected scene (~10 km strip).

Next we investigate the characteristics of the measured ARES channel data. The ARES thermal IR channel data exhibit characteristics of linearity in the two-channel radiance correlation as implied in Eq. (3). Figure 7 shows the scatter diagram for the three pairs of ARES channels: 61-60, 62-60, and 63-60. In each frame, the curve which is nearly linear denotes the correlation of Planck functions for the two channels, and the dots are radiance data points chosen from the scene of Fig. 5 covering the area of the strong contrast between clear and cloudy regions. The manner in which radiance data points distribute in clusters indicates a statistically significant linear correlation between each pair of channel radiances. There are two clusters in each frame. The upper cluster corresponds to clear data points, while the lower elongated clusters are associated with cloudy radiances.

Figure 8 demonstrates the comparability of the measured and computed $3.7\text{ }\mu\text{m}$ channel radiances for the retrieval of mean effective sizes. In the upper panel, the computed $3.7\text{ }\mu\text{m}$ solar radiances are plotted as functions of optical depth and six mean sizes. For $\tau > 2$, these radiances are nearly independent of the optical depth, but are strong functions of the ice crystal size distribution. In the middle panel, the computed $3.7\text{ }\mu\text{m}$ thermal IR radiances for different sizes are plotted against the optical depth. In this case, the cloud temperature is 250 K and the clear brightness temperature is 291 K. The $3.7\text{ }\mu\text{m}$ thermal IR radiances decrease with increasing optical depth and mean effective size. Finally, in the lower panel, the computed $3.7\text{ }\mu\text{m}$ total radiances are plotted against the optical depth for the six ice crystal sizes. It is

noted that these radiances are sensitive to both the optical depth and ice crystal size. We display the ARES measured data collected during the Track 3 of the September 16 flight on the lower diagram and show that they lie within the bulk range of the computed curves, indicating that it is feasible to use the ARES measured data to retrieve ice mean effective sizes.

Applying the retrieval scheme to the detected cloudy-pixel radiance data of the selected ARES channels, we can determine the cirrus cloud temperatures and emissivities (optical depth) for the four flight tracks of September 16, 1995. By using an efficient numerical scheme, the total run time on a powerful state-of-the-art SGI is less than 10 min for each track. For the purpose of displaying data, we obtain the array-averaged channel equivalent brightness temperatures and the retrieved parameters for each scan within the flight track. Variation of the computed array-averaged Ch. 60 equivalent brightness temperatures, cloud temperatures, optical depths, and mean effective sizes for Track 1 is shown in Fig. 9 based on the application of the retrieval scheme to 10^4 scans of the 45-pixel array data. There are three periods which have been identified as clear (~16-20 km, 25-28 km and 30-32 km). The retrieved cloud temperatures, optical depths, and mean effective ice crystal sizes vary between 230 and 260 K, between 0 and 2, and between 25 and 75 μm , respectively. Further examination of these retrieval results reveals that the cirrus cloud optical depths were generally less than 1.0, while the cirrus cloud temperatures were mostly higher than -30°C . The cirrus clouds were found to be composed of relatively small ice crystals. It is possible that these cirrus clouds were undergoing through a formation stage, during which ice crystal sizes are usually small and clouds are optically thin. The reliability of the aforementioned retrieval results has been confirmed by the following validation efforts.

3.4 Validation of Retrieval Results

To validate the retrieved cirrus cloud temperature/height, we use the time series of cloud boundary (cloud top and base) altitudes derived from the 8.6-mm radar measurements, together with the upper tropospheric temperature measurement by the Rosemount total temperature sensor on board the HARP. Figure 10(a) shows the atmospheric temperature at various levels between 5 and 11 km. These temperature values were obtained between 2029 and 2341 UTC. They vary between -5° and -55°C

within the altitude range. This temperature profile is used in the validation effort because there was no surface sounding launched around the flight time of the WB-57F. We assume that the upper atmospheric thermal structure remained the same during the HARP flight period, so that the temperature profile shown in Fig. 10(a) is representative throughout this period. Figure 10(b) shows the temporal variation of the cirrus cloud boundary altitudes derived from the 8.6-mm radar measurements between 2000 and 2400 UTC. A single layer of cirrus cloud was present during this time period. Between 2000 and 2100 UTC, the observed cloud top and base were located at 8 and 6 km, respectively. After 2100 UTC, the cloud-top altitude fluctuates between 8 and 10 km, while the cloud base altitudes largely remains at 6 km, except for the period between 2130 and 2230 UTC. There are two clear/thin-cirrus episodes around 2100 and 2140-2200 UTC and one broken-cirrus period around 2210-2220 UTC. The retrieved cloud temperatures were converted into cloud altitudes using the temperature sounding shown in Fig. 10(a). For Tracks 1 and 3, when WB-57F flew over the radar site, the area happened to be clear, although the radar recorded very thin cirrus. Thus, comparison of the retrieved cloud altitudes with the radar data cannot be accomplished. For Tracks 5 and 8, the retrieved cloud temperatures over the radar site are -33° and -40°C , which correspond to 8.2 and 9.2 km, respectively (denoted by square boxes in Fig. 10(b)). Both altitudes are within the radar-derived cloud boundaries but near the cloud top at the particular WB-57F overpass time.

To verify the retrieved cirrus cloud optical depths and ice crystal mean effective sizes, we use the *in-situ* ice crystal size distributions obtained by the optical probes on board the HARP to compute the single-scattering properties of the ice crystals and to evaluate the *in-situ* mean effective size. A representative ice crystal size distribution has been constructed for each case by using the 2D-C probe measurements for ice crystals larger than $75\text{ }\mu\text{m}$, and an extrapolation technique for ice crystals smaller than $75\text{ }\mu\text{m}$ in a manner described in the following.

Among the cloud microphysic instruments on board HARP, the FSSP sizes the ice crystals from 1 to $96\text{ }\mu\text{m}$; the 1D-C probe samples ice crystals from 20 to $300\text{ }\mu\text{m}$; and the 2D-C probe measures the maximum dimensions of the projection of ice crystals from 25 to $800\text{ }\mu\text{m}$. The size distributions derived

from the 1D-C and 2D-C probes closely agree with each other for the size range of 25 to 300 μm , though the differences in the ice crystal number concentrations for some size bins can be as large as one order of magnitude. We choose to use the 2D-C derived ice crystal size distribution because this probe covers the typical ice crystal size range and because the FSSP derived size distributions appear to be unreliable in view of the unrealistically high ice crystal number concentrations for sizes less than 20 μm . For these reasons, we use the Gamma function to extrapolate the 2D-C size distribution down to 1 μm to obtain the ice crystal size distribution for ice crystal sizes less than 75 μm (Tsay *et al.* 1996). Composite ice crystal size distributions combining the 2D-C probe measurements and the extrapolated portions are plotted in Fig.11 (a) and (b). The upper bound for both the ice crystal size distributions is less 600 μm . Both ice crystal size distributions are similar to those occurred in typical cirrostratus clouds (Heymsfield 1975). We find that incorporating the extrapolated portion from 20 μm down to 1 μm has negligible effects on the extinction coefficient. Other single-scattering parameters are not sensitive to the inclusion of ice crystals smaller than 75 μm for the size distributions used in the present study. Visible extinction coefficients of 0.54 and 0.57 km^{-1} were obtained for cases 1 and 2, respectively.

To determine the optical depth based on *in-situ* measurements, the average cirrus cloud thickness and the associated extinction coefficients must be known. Based on the cloud boundary altitudes derived from the 8.6-mm radar measurements, the averaged cirrus cloud thicknesses during the two periods were about 1.75 and 2 km for cases 1 and 2, respectively. The ascending vertical profile of the 2D-C median volume ice crystal diameter indicates that ice crystal sizes vary by no more than 20 μm between 6.5 and 8 km (Morrison *et al.* 1997). For this reason, we use the computed extinction coefficients based on single-level *in-situ* size distributions to represent the vertically averaged cirrus cloud extinction coefficients. The computed optical depths based on the preceding approximation are 0.94 and 1.14 for cases 1 and 2, respectively. The mean retrieved optical depths are 0.89 and 1.42 for Tracks 1 and 3 of the ARES flight, respectively. The retrieved mean optical depth for Track 1 agrees relatively well with that from the 2D-C probe. However, for Track 3, the difference between the two optical depths is on the order of 0.3.

Finally, we utilize a cirrus cloud model composed of 50% bullet rosettes, 30% hollow columns, and 20% plates to compute the *in-situ* mean effective ice crystal sizes. An empirical relationship between the maximum dimension (L) and width (W) is employed for each shape: for plates, $W = 2.02 \cdot L^{0.449}$; for hollow columns, $W = 11.3 \cdot L^{0.414}$ for $L > 200 \mu\text{m}$, $W = 8.479 + 1.002 L - 0.00234 L^2$ for $L < 200 \mu\text{m}$; and for bullet rosettes, $W = 2.3103 L^{0.63}$. The *in-situ* mean effective sizes are based on the average of the mean effective size for each shape weighted by the percentage distribution. They are $57.2 \mu\text{m}$ for case 1 and $55.2 \mu\text{m}$ for case 2. The retrieved mean effective sizes are $64.2 \mu\text{m}$ for Track 1 and $53.3 \mu\text{m}$ for Track 3, which compare reasonably well with the *in-situ* sizes with differences less than $10 \mu\text{m}$. There are two reasons for differences between retrieved and observation-derived optical depths and mean effective sizes. First, estimate of the optical depth from the 2D-C probe is based on the composite ice crystal size distribution at a single flight level within the cirrus cloud. Second, the variation range of the retrieved optical depth for Track 3 is much larger than that for Track 1.

4. Summary

We have presented a remote sensing algorithm for the retrieval of cirrus cloud temperature (height), optical depth, and ice crystal size using, for the first time, the spectral channels in the $5.1\text{-}5.3 \mu\text{m}$ range in combination with the $3.7 \mu\text{m}$ channel. This scheme has been applied to the ARES data collected on September 16, 1995, over the western Boston area. We have discussed the ARES channel spectral properties and the rationale for the selection of retrieval channels. Characteristics of the measured ARES channel data have been examined to demonstrate their suitability for retrieval. For retrieval purposes, a simple clear/cloud threshold detection scheme has been developed and applied to identify clear and cloudy data points.

Validation of the retrieved cirrus cloud temperature/height has been carried out by using the collocated and coincident time series of the cloud boundary (cloud top and base) altitudes derived from the ground-based 8.6 mm radar measurements. We have also compared the retrieved cirrus cloud optical depths and ice crystal mean effective sizes with those parameters determined based on the composite ice

crystal size distributions from *in-situ* measurements. We show that the retrieved cloud heights compare reasonably well with the values determined from the ground-based 8.6-mm radar, and that the retrieved optical depth and mean effective size match the values determined from the *in-situ* microphysical measurements. Differences between the retrieved and observation-derived optical depths and mean effective sizes could be due to the limitation in data collection by aircraft and the inherent cloud horizontal and vertical inhomogeneity.

Acknowledgements. During the course of this work, our research programs have been supported by the Air Force Geophysical Directorate under Contract F19628-96-C-0052, and in part by the AFOSR grant F49620-94-1-0142, and NASA Grants NAG5-6160 and NAG5-6036.

REFERENCES

- Anderson, G. P., R. H. Picard, and J. H. Chetwind, "Proceedings of the 17th Annual Review Conference on Atmospheric Transmission Models", Special Report No. 274, 332pp, Phillips Laboratory/Geophysics Directorate, MA. May 1995.
- Baum, B. A., R. F. Arduini, B. A. Wielicki, P. Minnis, and Si-Chee Tsay, Multilevel cloud retrieval using multispectral HIRS and AVHRR data: Nighttime oceanic analyses. *J. Geophys. Res.*, **99**, 5499-5514, 1994.
- Fu, Q., and K. N. Liou, Parameterization of the radiative properties of cirrus clouds. *J. Atmos. Sci.*, **50**, 2008-2025, 1993.
- Gao, B. C., and Y. J. Kaufman, Selection of a 1.375- μm channel for remote sensing of cirrus clouds and stratospheric aerosols from EOS/MODIS. *J. Atmos. Sci.*, **52**, 4231-4237, 1995.
- Goody, R. M., and Y. L. Yung, *Atmospheric Radiation Theoretical Basic*, 2nd Ed., Oxford University Press, New York, 519pp, 1989.
- Heymsfield, A., Cirrus uncinus generating cells and the evolution of cirriform clouds. Part I: Aircraft observations of the growth of ice phase. *J. Atmos. Sci.*, **32**, 799-808, 1975.
- King, M. D., Y. J. Kaufman, W. P. Menzel, and D. Tanre, Remote sensing of cloud aerosol, and water vapor properties from the Moderate Resolution Imaging Spectrometer (MODIS), *IEEE Trans. Geosci. Remote Sensing*, **30**, 1-27, 1992.
- King, M. D., W. P. Menzel, and co-authors, 1995 : Airborne scanning spectrometer for remote sensing of cloud, aerosol, water vapor and surface properties, *J. Atmos. Oceanic Tech.*, **13**, 777-794.
- Liou, K. N., *Radiative and Cloud Processes in the Atmosphere: Theory, Observation, and Modeling*. Oxford University Press, New York, 487 pp, 1992.
- Liou, K. N., S. C. Ou, Y. Takano, F. P. J. Valero, and T. P. Ackerman, Remote sounding of the tropical cirrus cloud temperature and optical depth using 6.5 and 10.5 μm radiometers during STEP. *J. Appl. Meteor.*, **29**, 716-726, 1990.
- Minnis, P., D. F. Young, K. Sassen, J. M. Alvarez, and C. J. Grund, The 27-28 October 1986 FIRE IFO cirrus case study: Cirrus parameter relationships derived from satellite and lidar data. *Mon. Wea. Rev.*, **118**, 2402-2425, 1990.
- Minnis, P., K. N. Liou, and Y. Takano, Inference of cirrus cloud properties from satellite-observed visible and infrared radiances. *J. Atmos. Sci.*, **50**, 1279-1322, 1993.
- Morrison, B. J., R. Hobbs, D. Rusk, J. Jung, and R. L. Rose. *The High-Altitude Reconnaissance Platform (HARP)*, SBIRS Final Report, Aeromet, Inc., 264 pp., 1997.
- Ou, S. C., K. N. Liou, W. M. Gooch, and Y. Takano, Remote sensing of cirrus cloud parameters using AVHRR 3.7- and 10.9- μm channels. *Appl. Opt.*, **32**, 2171-2180, 1993.

- Ou, S. C., K. N. Liou, and Co-authors, Remote sounding of cirrus cloud optical depths and ice crystal sizes from AVHRR data: verification using FIRE II IFO Measurements. *J. Atmos. Sci.*, **52**, 4143-4158, 1995.
- Rao, N. X., S. C. Ou, and K. N. Liou, Removal of the solar component in AVHRR 3.7- μ m radiances for the retrieval of cirrus cloud parameters. *J. Appl. Meteor.*, **34**, 482-499, 1995.
- Takano, Y., and K. N. Liou, Radiative transfer in cirrus clouds, II. Theory and computation of multiple scattering in an anisotropic medium. *J. Atmos. Sci.*, **46**, 20-36, 1989.
- Tsay, S.-C., P. M. Gabriel, M. D. King, and G. L. Stephens, 1996 : Spectral reflectance and atmospheric energetics in cirrus-like clouds. Part II : Applications of a Fourier-Riccati approach to radiative transfer. *J. Atmos. Sci.*, **53**, 3450-3467.
- Wielicki, B. A., P. Minnis, R. F. Arduini, L. Parker, S.-C. Tsay, Y. Takano, and K. N. Liou, Remote sensing estimates of cirrus particle size for tropical and midlatitude cirrus: Hexagonal crystals and ice spheres, in *Proceedings of the FIRE Cirrus Science Conference*, pp. 201-204, Breckenridge, Colorado, June 14-17, 1993.
- Yang, P., and K. N. Liou, Finite-difference time domain method for light scattering by small ice crystals in three-dimensional space. *J. Opt. Soc. Am. A.*, **13**, 2072-2085, 1996a.
- Yang, P., and K. N. Liou, Geometric-optics-integral-equation method for light scattering by nonspherical ice crystals. *Appl. Opt.*, **35**, 6568-6584, 1996b.

FIGURE CAPTIONS

- Fig. 1. The k -value as a function of D_e for the retrieval channels. Eleven size distributions have been used for single-scattering computations. The single-scattering properties are used in an adding/doubling code to obtain the cloud emissivity.
- Fig. 2. A schematic flow chart for the cirrus retrieval algorithm using ARES channel data.
- Fig. 3. Upwelling radiances for solar reflection and thermal emission in the $2\text{--}6.5\ \mu\text{m}$ region. F denotes the solar irradiances, μ is the cosine of solar zenith angle, α is the surface albedo, and B_λ is the Planck function.
- Fig. 4. Typical ARES 75-channel spectra for clear and cloudy areas.
- Fig. 5. Radiance images for ARES Chs. 41, 42, 55, 60, and 63 over a selected scene having a strong cloud/clear contrast within the Track 1 of September 16 flight.
- Fig. 6. Histograms of the brightness temperatures for the ARES Chs. 60-63 within the domain of Fig. 7.
- Fig. 7. Examples of the scatter diagram for three pairs of ARES channels: 60-61, 60-62, and 60-63.
- Fig. 8. Computed $3.7\ \mu\text{m}$ solar radiances (a), IR radiances (b), and total radiances (c) as functions of optical depth and ice crystal size.
- Fig. 9. Array averaged channel equivalent brightness temperatures, retrieved cloud temperature, cloud optical depth, and effective size as functions of flight distance for Track 1, 9/16/95.
- Fig. 10. (a) Partial sounding of the middle and upper troposphere, obtained from the HARP flight above Hanscom AFB (squares correspond to the retrieved cloud temperature). (b) Comparison of the cloud top heights obtained from radar/lidar measurements and the retrieved cloud temperatures. Retrieved temperatures are displayed for Tracks 1, 3, 5, and 8 (in chronological order).

Fig. 11. The ice crystal size distributions based on the HARP data (9/16/95) with the lower limit of 75 μm and extrapolations to 20 μm and 1 μm based on the Gamma function and an optimization search method.

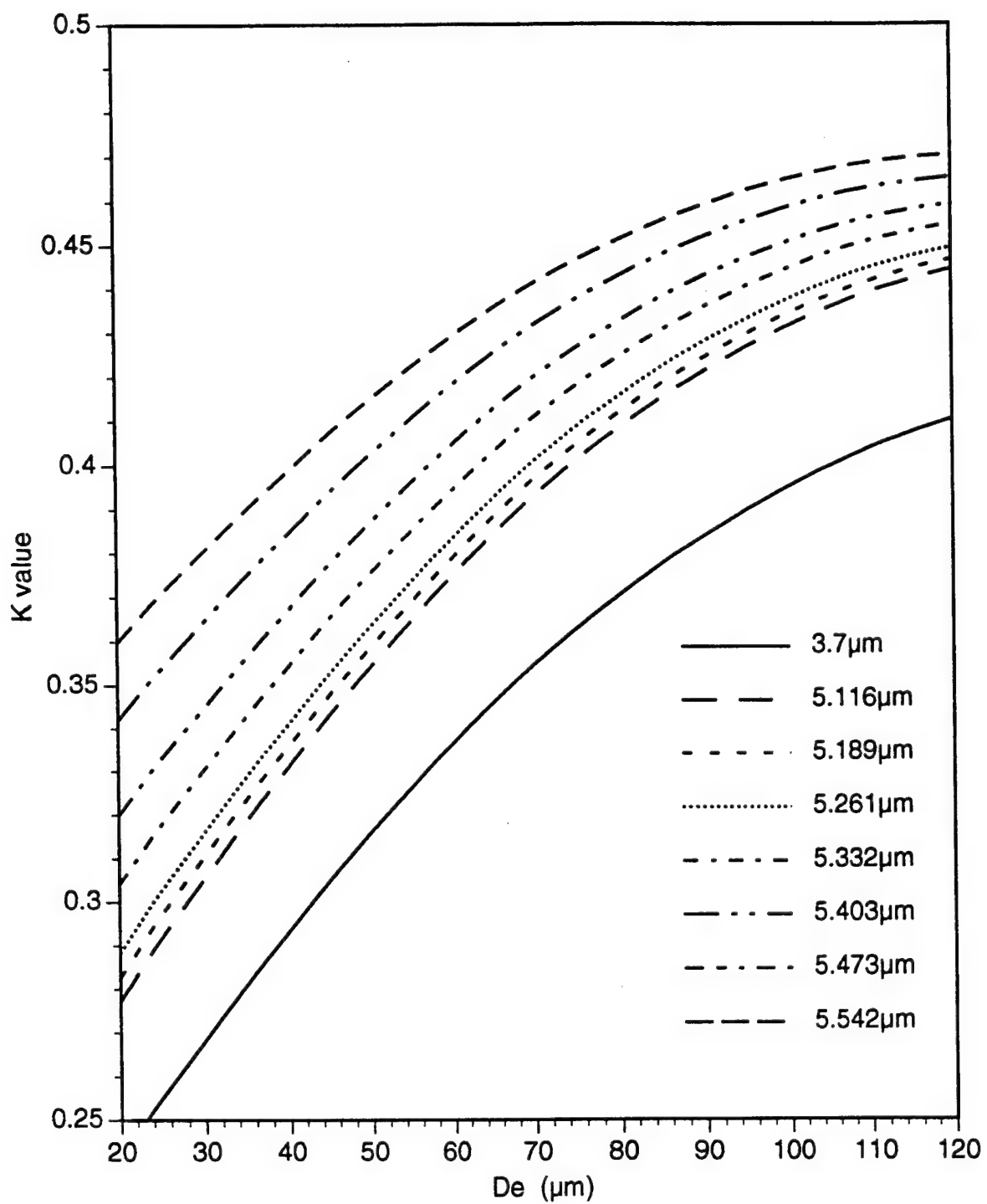


Fig.1

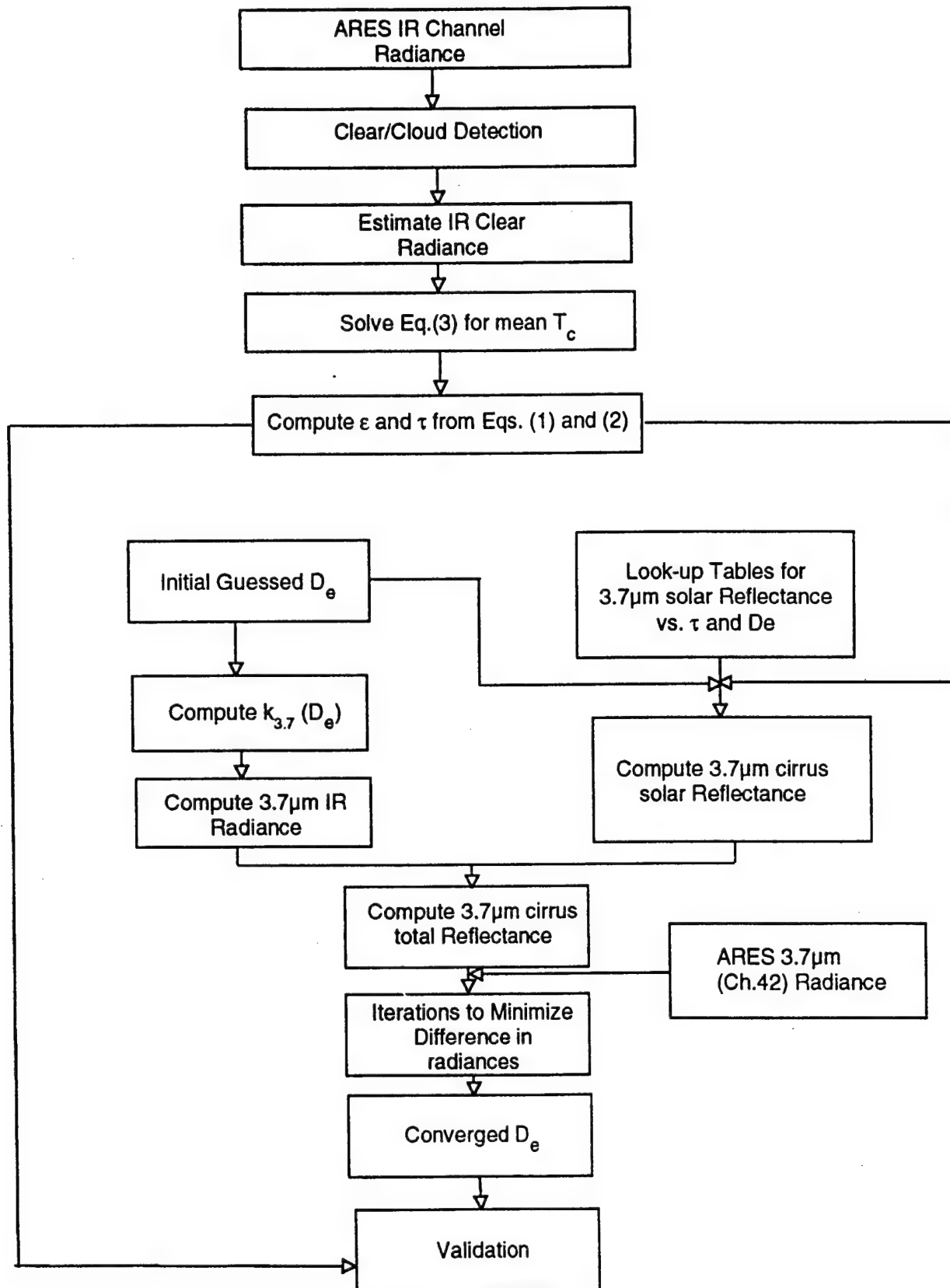
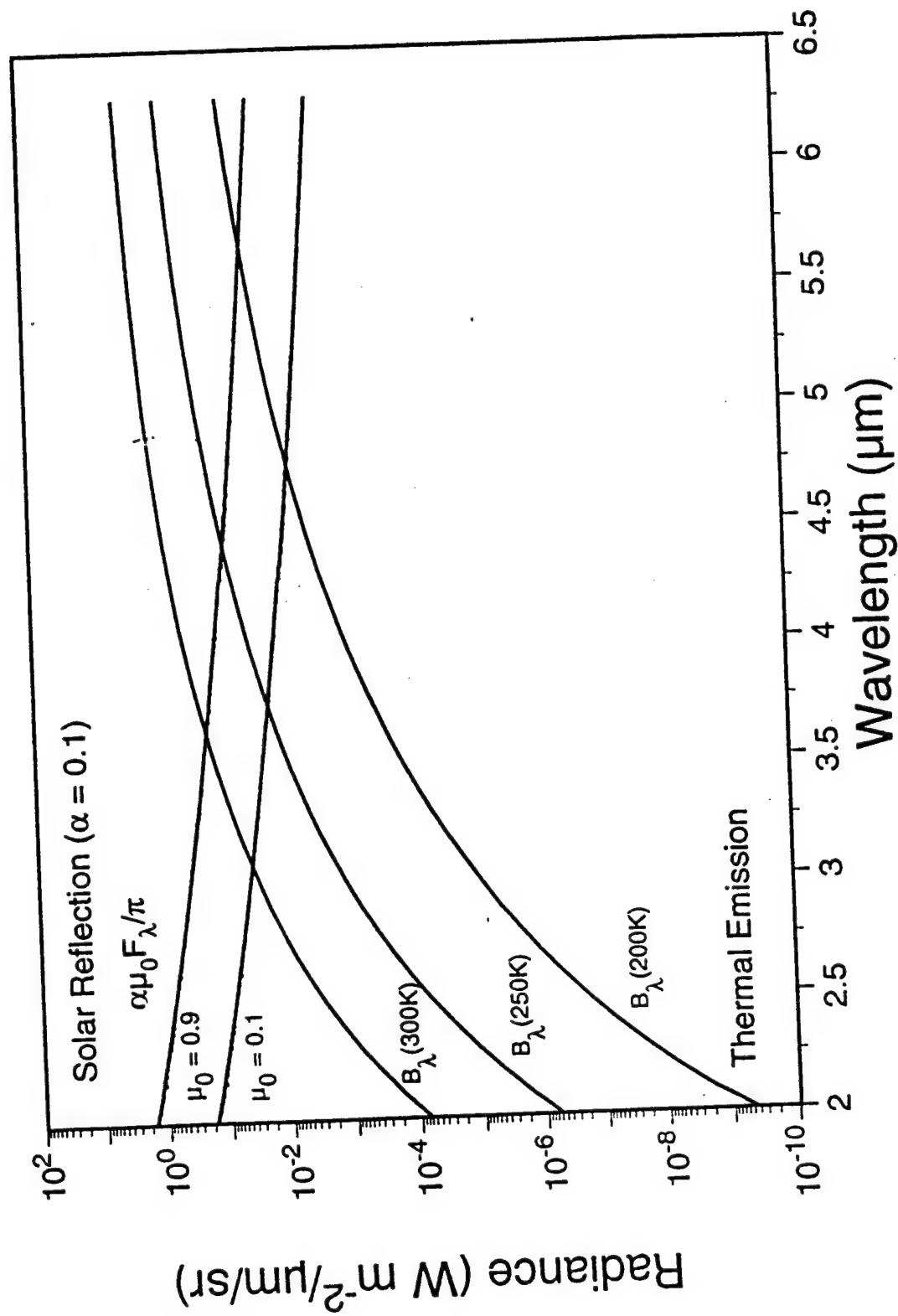


Fig. 2



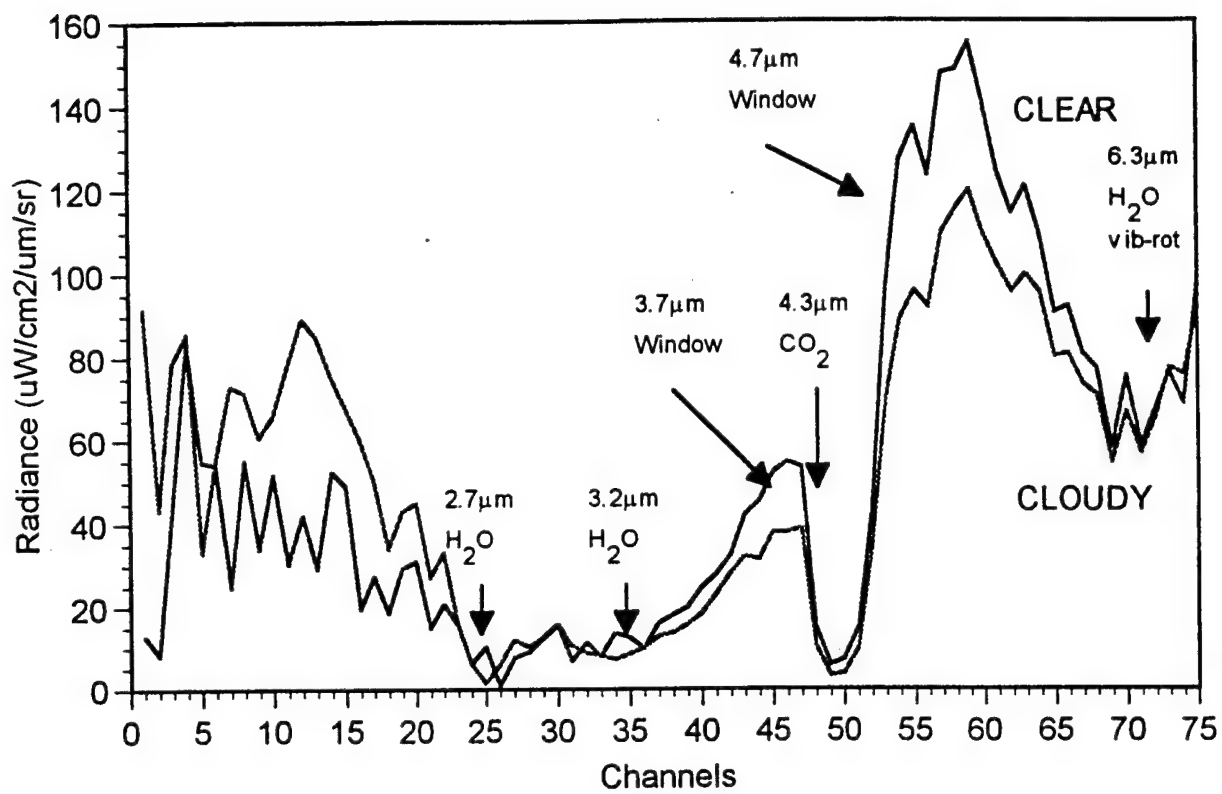


Fig. 4

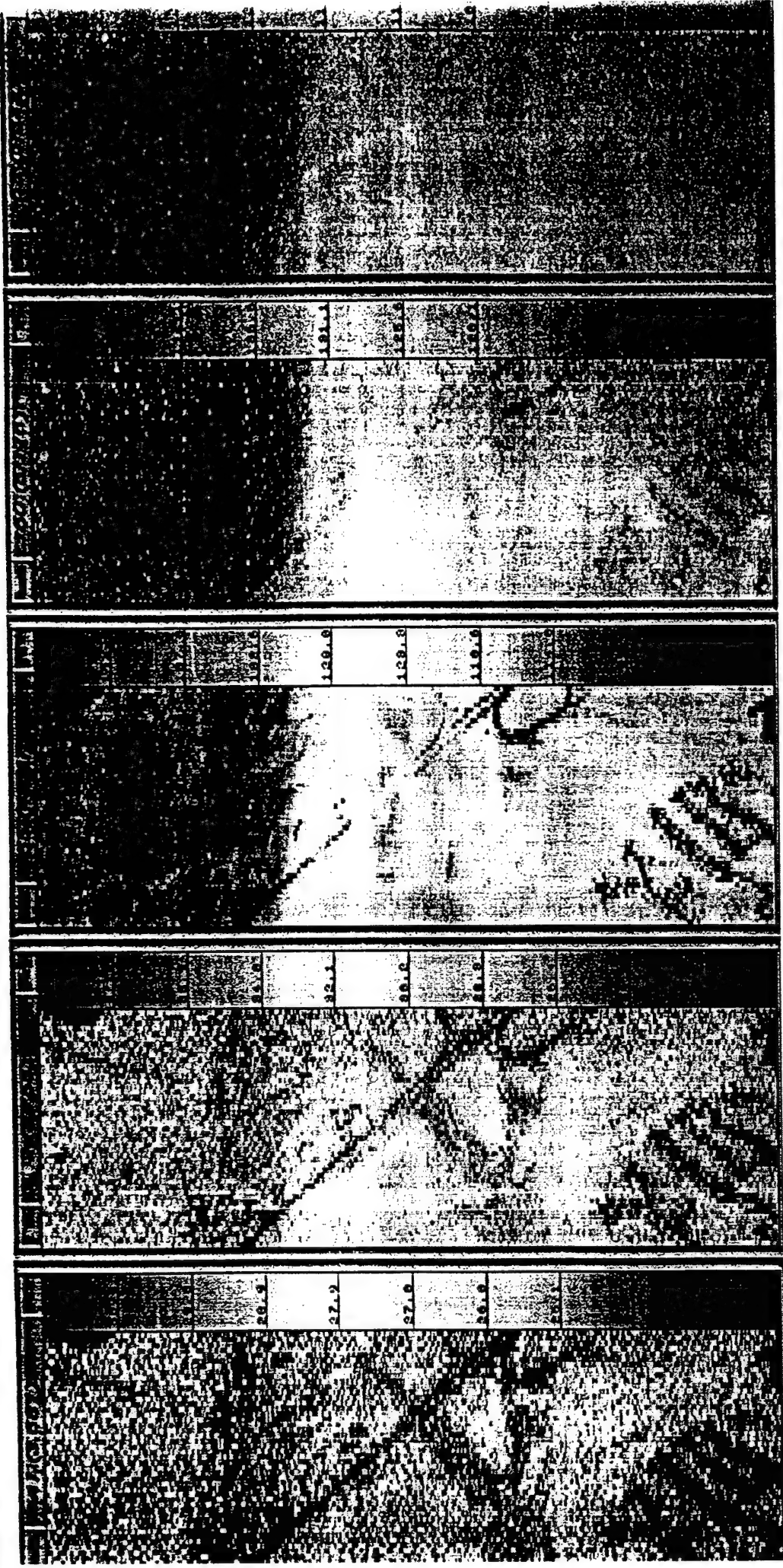


Fig. 5

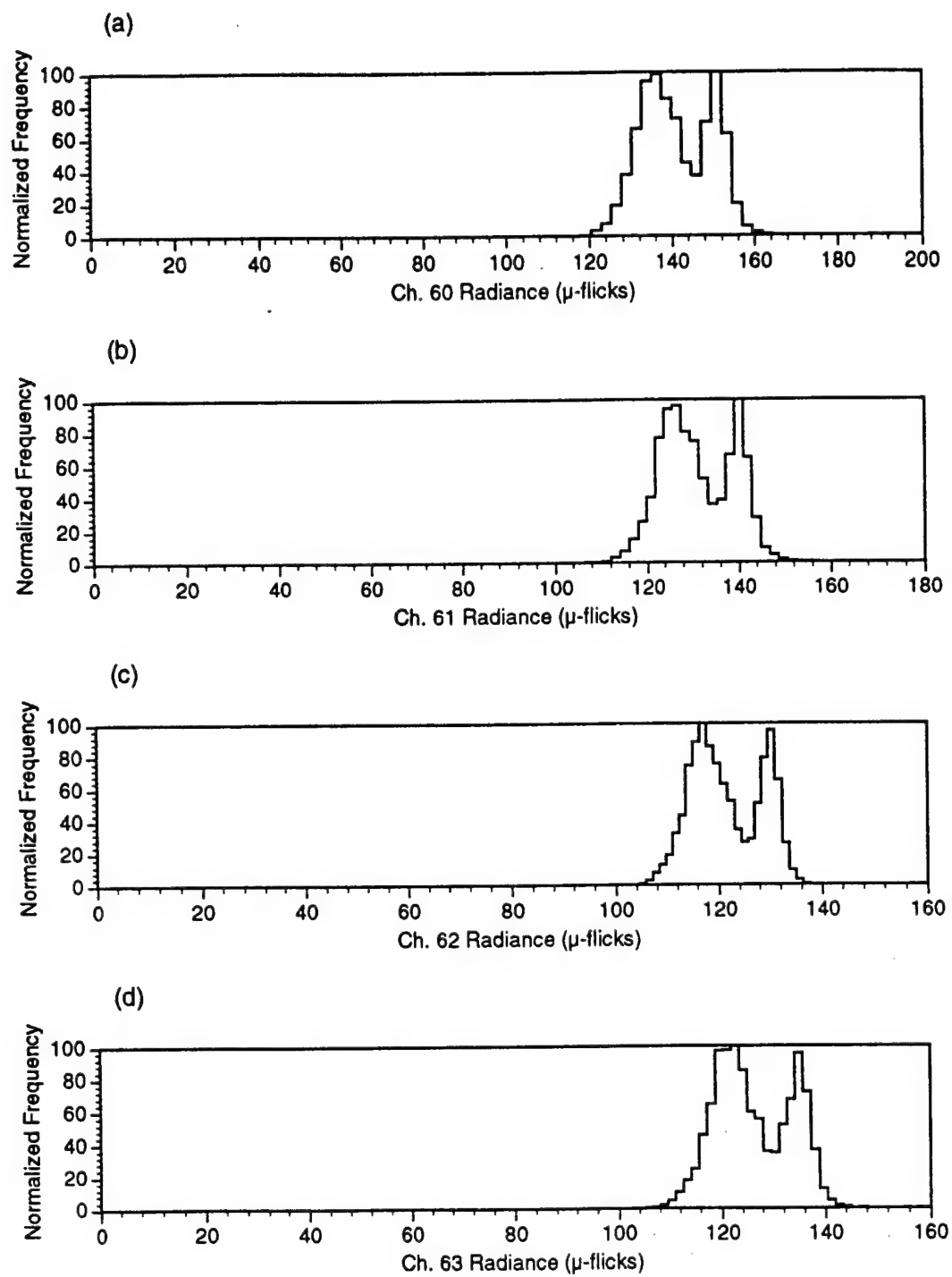


Fig. 6

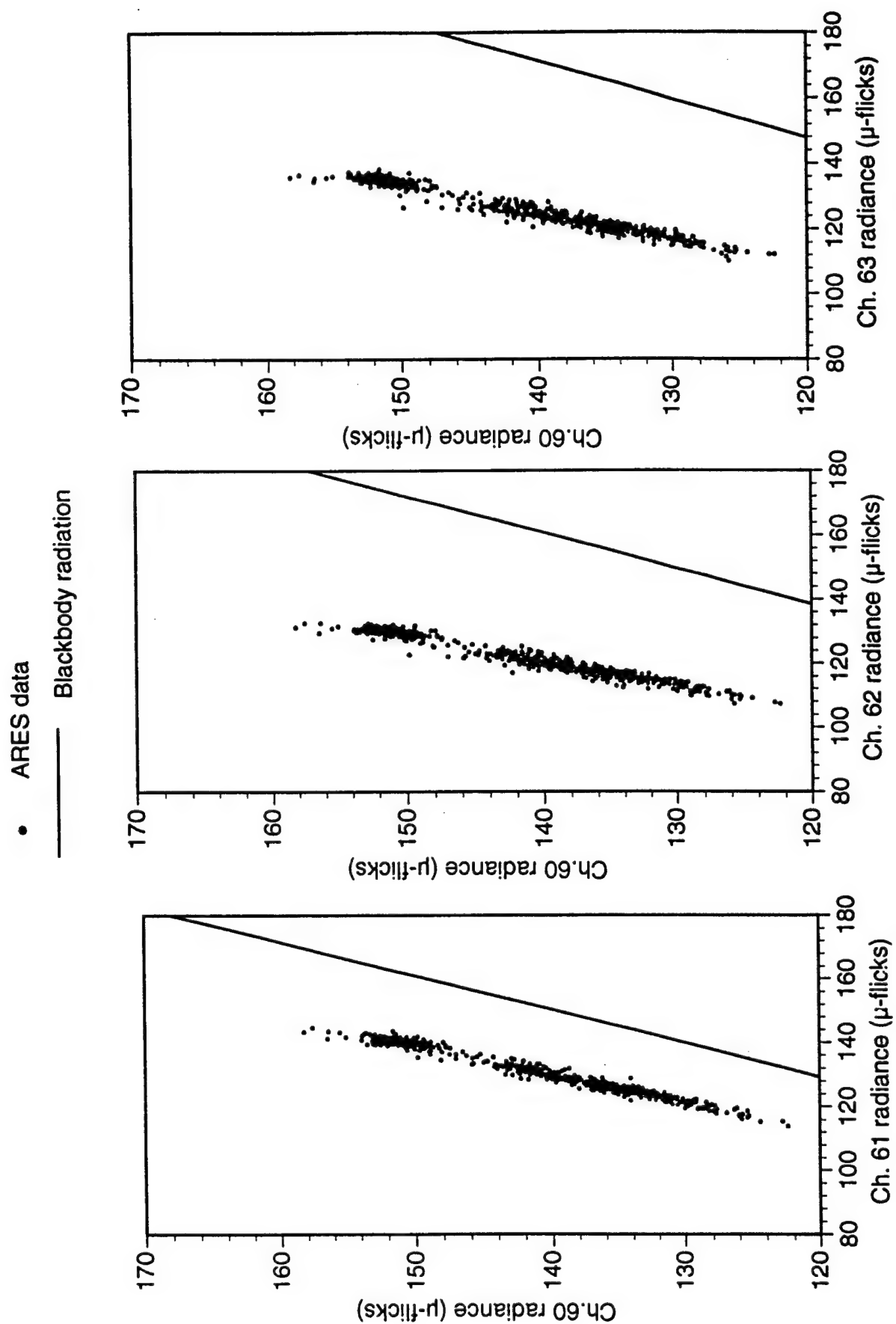


Fig. 7

COMPUTED SOLAR/IR/TOTAL RADIANCES FOR ARES CHANNEL 42
Flt. 091695 TRACK3

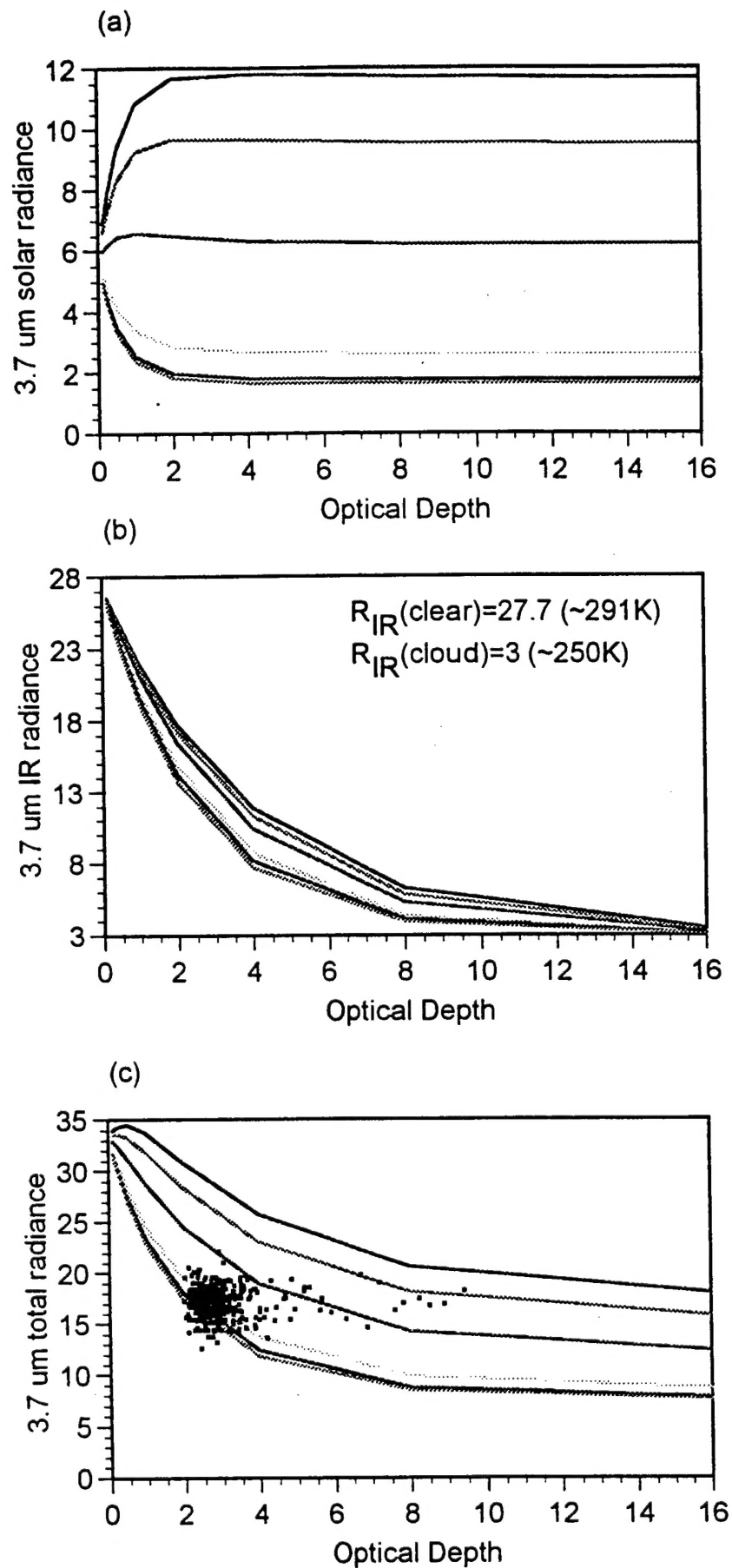


Fig. 8

ARES Flt. 091695 TRACK 1

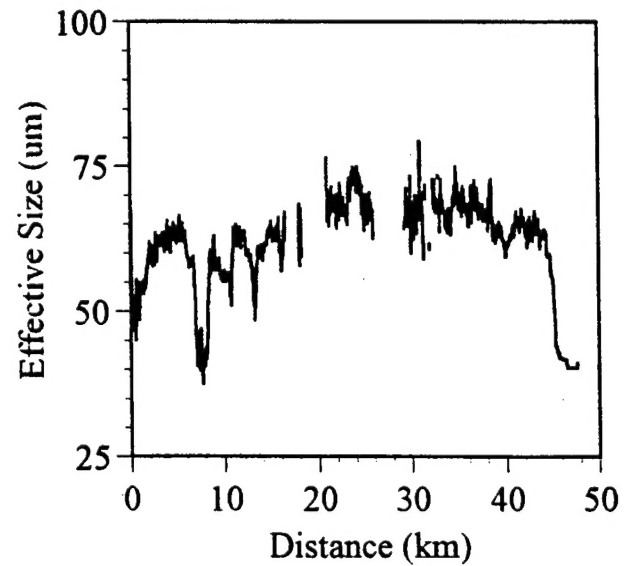
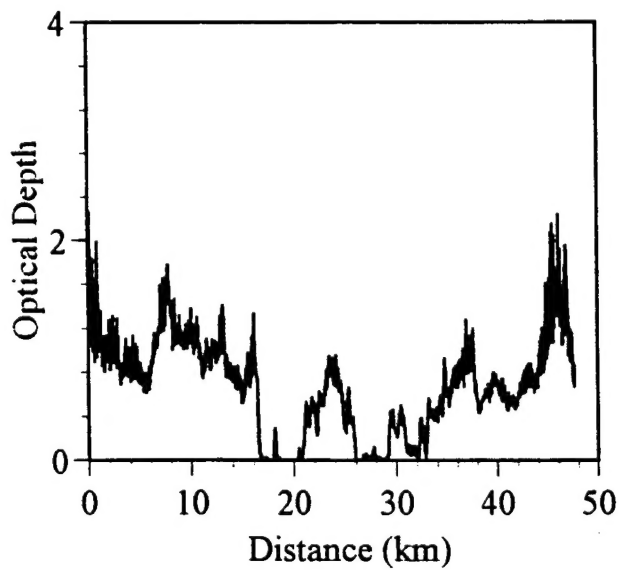
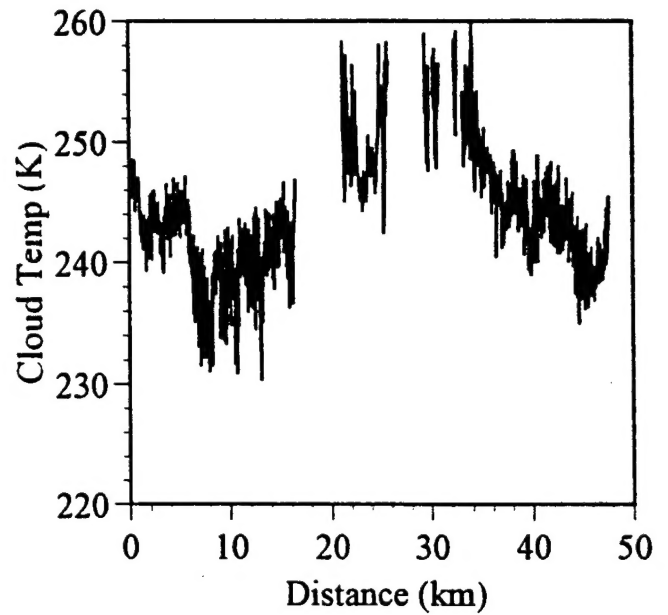
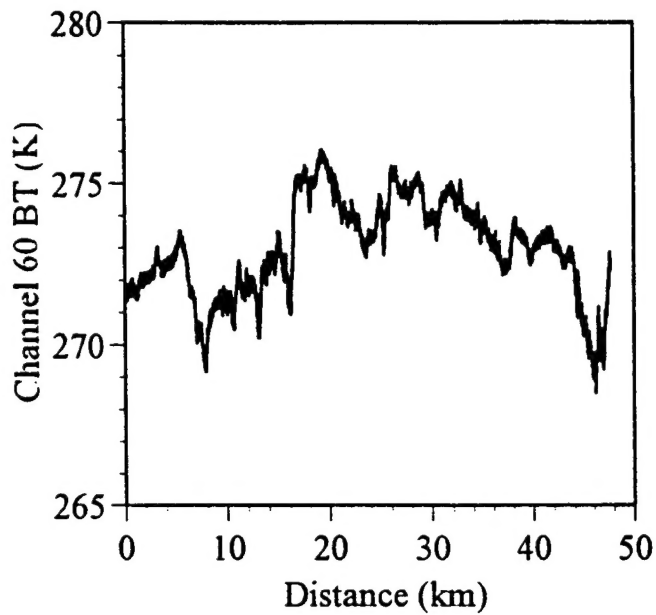


Fig. 9

ARES Flt. 091695

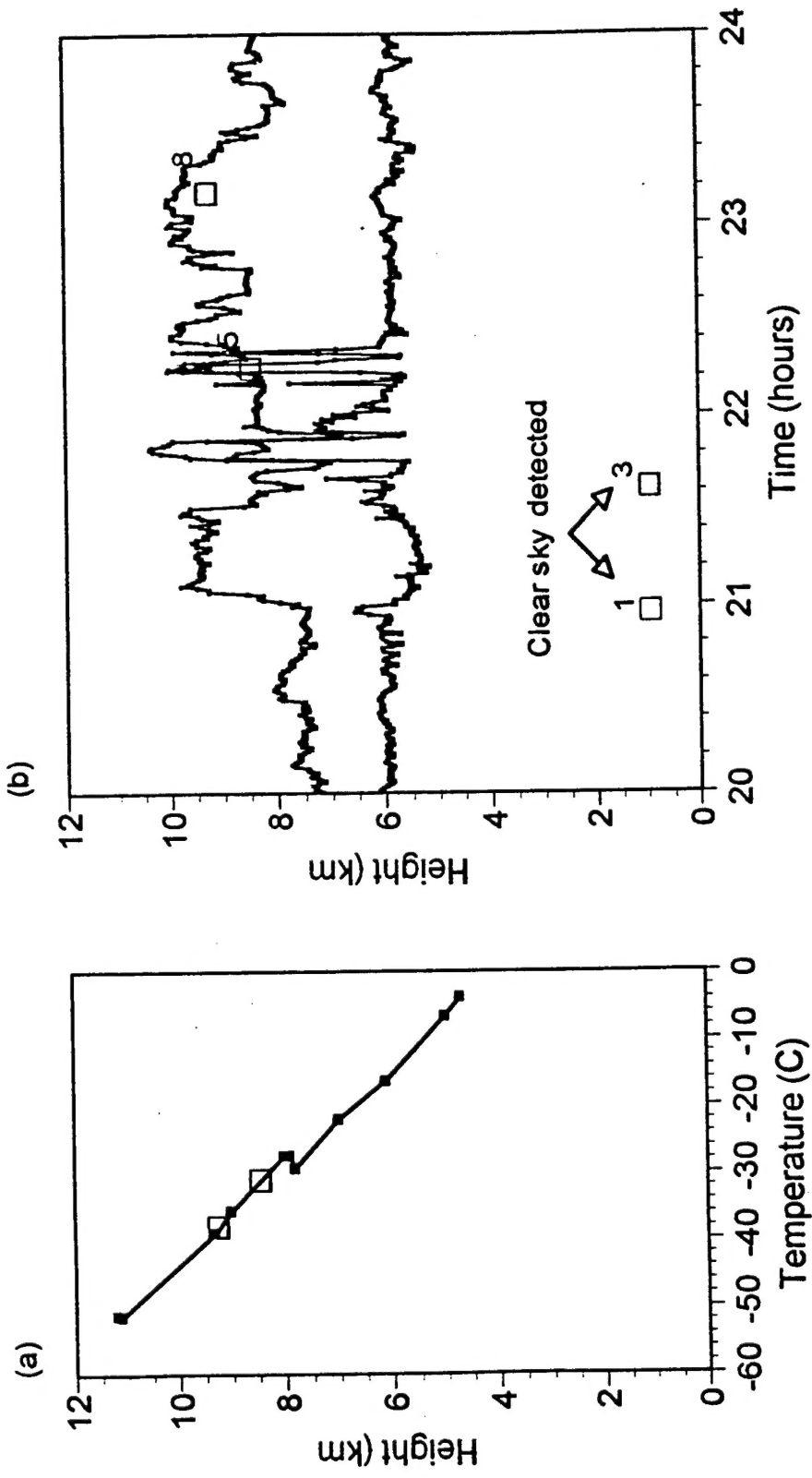


Fig. 10

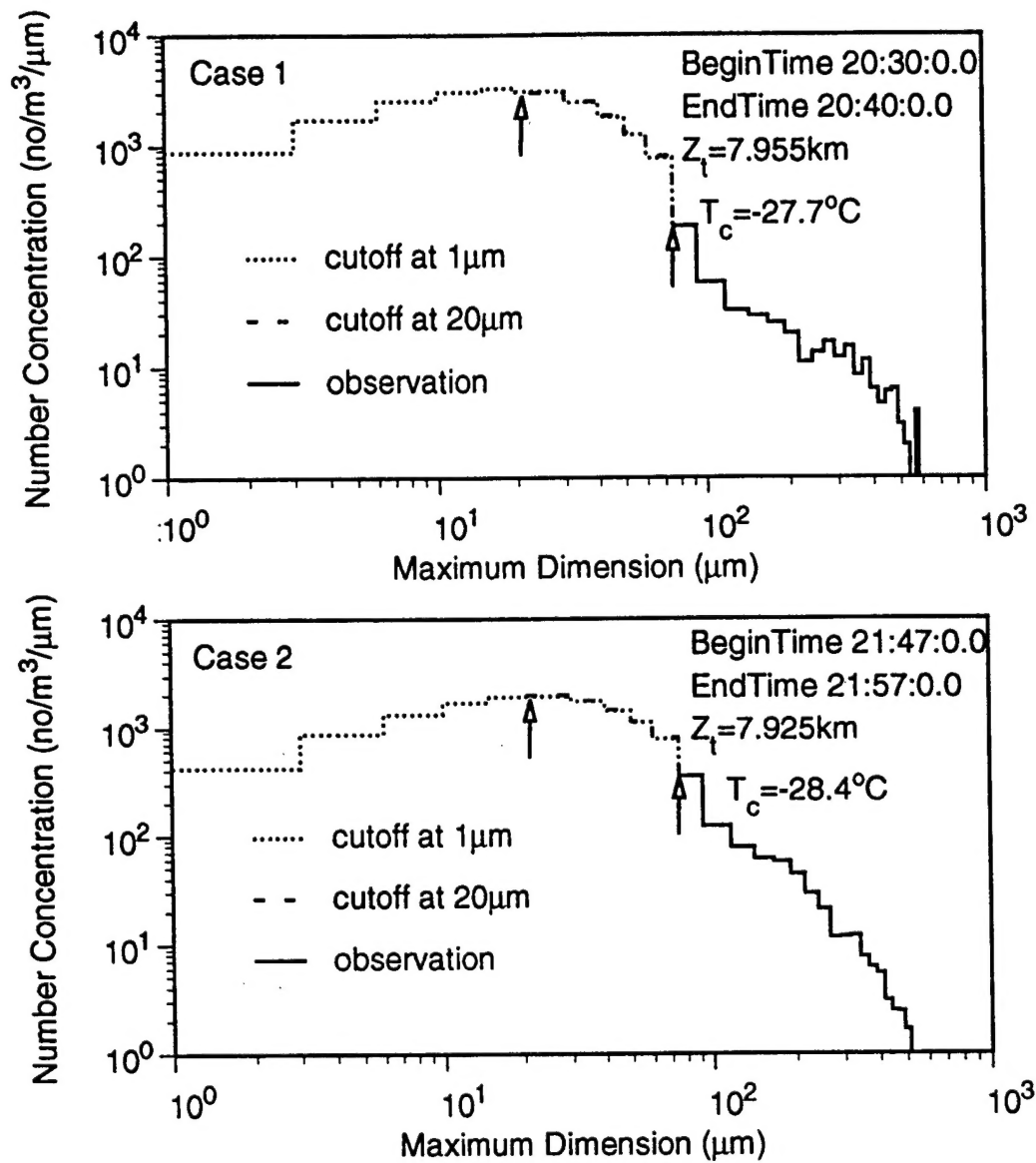


Fig.11